TÉCNICO LISBOA

Development of an Enhanced Actuator Disc Model for the Simulation of Wind Farms

Asif Zubair

Thesis to obtain the Master of Science Degree in

Energy Engineering and Management

Supervisors: Prof. José Alberto Caiado Falcão de Campos
Dipl.-Ing. Matthias Kretschmer

Examination Committee

Chairperson: Prof. Edgar Caetano Fernandes
Supervisor: Prof. José Alberto Caiado Falcão de Campos
Member of the Committee: Prof. Luís Rego da Cunha Eça

November 2016

ACKNOWLEDGEMENT

First of All, I would like to thank KIC InnoEnergy for giving me the opportunity for valuable M.Sc. ENTECH program. By completing this program, I have reached an important milestone in my life of doing a master degree in the field of energy.

Secondly, I would like to extend words of thanks to my thesis supervisor Prof. José Alberto Caiado Falcão de Campos at IST for approving this thesis and allowing me to conduct this thesis at Stuttgart Wind Energy (SWE) at Stuttgart University. His lectures in the course of “Offshore wind energy” were a major stimulation for me to pursue my master thesis in the field of aerodynamics of wind turbines. His immense support, patience, motivation and knowledge throughout the course of my thesis has helped me a lot in conducting and finishing the master thesis.

Further, I would like to thank my thesis supervisor Dip.- Ing Matthias Kretchhmer at SWE for giving me the wonderful opportunity of this master thesis in his institute. I express my sincere gratitude to him for helping me understand the thesis, guiding me at each and every turn of the thesis, sharing his knowledge with me over the subject and for being patient in answering all my questions.

Lastly, I would like to thank Prof. Chen and his entire team for allowing me to use the resources of his institute, including computer labs, for my thesis and providing supportive and friendly atmosphere for work at all times during the course of my thesis.

ABSTRACT

Computational Fluid Dynamics (CFD) is one of many tools available for predicting the performance and the flow characteristics around a horizontal axis wind turbine. CFD simulations of a fully resolved turbine geometry gives good results but it is computationally very expensive. An alternate approach is to use a simplified CFD-BEMT approach in which the turbine is replaced by an actuator disc and coupled to the Blade Element Momentum Theory (BEMT). The blades of a wind turbine generate tip vortices. These tip vortices reduce the lift and hence efficiency, particularly near the tip region. The CFD-BEMT model is not capable of capturing the effect of the tip vortices on the performance as well as on the flow field. In this master thesis, three enhanced actuator disc models are presented which are developed by combining BEMT with Lifting Line Theory (LLT) and coupling them to CFD. The three methods use different approaches to combine BEMT with LLT. Simulations are performed for CFD-BEMT, with and without the Prandtl tip loss factor, and with the three enhanced actuator disc models and results are produced for the performance of the turbine as well as for the flow field. The Performance result are compared with the results obtained from the FAST V8 code and the local flow field results are compared with the results obtained from the LLT IST code. The results show that none of the enhanced actuator disc models is capable of accurately predicting performance and the local flow field simultaneously.

Keywords: Computational Fluid Dynamics (CFD), Blade Element Momentum Theory (BEMT), flow field, Lifting Line Theory (LLT), tip vortices.

RESUMO

A Mecânica dos Fluidos Computacional (CFD) é uma das ferramentas disponíveis para prever o desempenho e as características do escoamento de uma turbina eólica de eixo horizontal (HAWT). A simulação de CFD-RANS de uma turbina de geometria 3D completamente discretizada é muito exigente em termos computacionais. Uma abordagem alternativa é a utilização de um modelo de disco atuador com a Teoria do Momento do Elemento de Pá (BEMT). Este modelo de CFD-BEMT não é capaz de considerar o efeito de vórtices de ponta. Nesta tese de mestrado, três modelos melhorados de discos atuadores são apresentados,através da combinação de BEMT com a Teoria da Linha Sustentadora (LLT) e combinadas com o modelo de RANS. Os três métodos usam diferentes abordagens para combinar BEMT com LLT. As simulações são efetuadas para CFD-BEMT, com e sem fator de perda na ponta de Prandtl, e com os três modelos melhorados de disco atuador. Os resultados são produzidos para o desempenho da turbina, bem como para o campo de escoamento. O resultado de desempenho desse modelo é comparado com o resultado obtido a partir do código FAST V8 e os resultados de campo de escoamento comparados com os resultados do código LLT. Os resultados mostram que nenhum dos modelos de disco atuador melhorado é capaz de prever simultaneamente de forma correta o desempenho da turbina e o campo de escoamento. Quando há uma melhoria na previsão do desempenho, há uma deterioração da previsão do campo de escoamento, e vice versa.

Palavras-chave: Mecânica dos Fluidos Computacional (CFD), Teoria do Momento do Elemento de Pá (BEMT), Campo de escoamento, Teoria da linha Sustentadora (LLT), Vórtice de ponta

TABLE OF CONTENTS

LIST OF TABLES

LIST OF FIGURES

NOMENCLATURE

U	Incoming free stream air velocity
U_{rel}	Relative velocity of air
v_a	Axial induced velocity
v_t	Tangential induced velocity
a	Axial induction factor
b	Tangential induction factor
λ	Tip speed ratio
λr	Local speed ratio
A	Axial force (Thrust force)
T	Tangential force
Q	Torque
P	Power
C_T	Coefficient of Thrust
C_P	Coefficient of Performance
C_L	Coefficient of lift
C_D	Coefficient of drag
ω	Angular velocity of flow stream
Ω	Angular velocity of wind turbine rotor
ρ	Density of air
c	Chord length
ψ	Pitch
B	Number of blades
ϕ	Undisturbed flow inclination angle
φ	Induced flow inclination angle
ε	Drag to lift ratio
Γ	Circulation
r_h	Hub radius
R	Turbine tip radius
F	Prandtl tip loss correction factor
Δx	Thickness of actuator disc
ST_{ax}	Momentum source term axial
ST_{tan}	Momentum source term tangential
AST_{ax}	Additional momentum source term axial
AST_{tan}	Additional momentum source term tangential
A_S	Swept area of rotor
Re	Reynolds number

CHAPTER 1: INTRODUCTION

1.1 Background

Wind has powered the ships since as early as 5000 B.C [16]. Windmills have been in use for more than 3000 years. Wind mills were mainly used for grinding grains and pumping water [6]. In the start of twentieth century, the use of electricity started growing and the windmills were slowly transformed into the wind turbines to generate electricity by connecting the rotor to the generator [10]. Wind power found new applications in powering buildings at remote sites [9]. Till 1960's, the wind turbines were of little importance for the production of electricity due to cheap availability of fossil fuels which were used to generate electricity from combustion engines [6].

After the oil crisis of 1973, the wind turbines got the attention of many countries which wanted to reduce their dependence on the imported fossil fuels and numerous research programs were launched across many countries in the field of wind power in search for harnessing wind power reliably and efficiently. Since the oil crisis, commercial wind turbines have steadily emerged as a significant business with an annual turnover in the 1990s of more than a billion US dollars per year. Since then this figure has increased by approximately 20% a year [6]. Today, the wind turbines are being produced in a variety of sizes. Their size and operation range from small standalone turbines for battery charging at isolated places to large multi megawatt machines as part of near-gigawatt-size wind farms that provide electricity to national electric transmission systems [9].

The wind turbines generate downstream wakes. When the wind turbines are put in a wind farm with limited area, power losses occur due to wakes. These losses vary with the arrangements of the wind turbines and the conditions of incoming wind [17]. Field experiments and computational fluid dynamics (CFD) have unanimously shown that the power produced by a wind farm is smaller than the combined rated powers of its constituent turbines. This is because a wind turbine extracts energy from freestream atmospheric flow. This generates a wake at the downstream side of the turbine with reduced velocity. This wake interacts with a downstream wind turbine and limits its power generation capacity [13]. Therefore, it is an absolute necessity to optimize the layout design of the wind farms that can minimize the wake losses and improve the energy production. The optimization of wind farm layout in turn depends on accurate modelling of the wind turbine performance as well as the flow field around and downstream of a wind turbine.

1.2 Motivation and Purpose

CFD simulations have the potential to simulate and predict the aerodynamic characteristics of a wind as well as the flow field characteristics around the turbine and in the wake region. CFD is necessary to visualize the details of the flow. However, simulating fully resolved 3D horizontal axis wind turbine (HAWT) geometry requires high computational power and time and hence is very expensive. An alternate approach is to use a simplified and mixed CFD-BEMT approach. In this approach, the Blade Element Momentum Theory (BEMT) is coupled to the Reynolds-Averaged Navier Stokes equations (CFD-RANS) using an actuator disc

concept. This simplified approach requires less computational power and time and hence is much more efficient [3], [8].

The BEMT assumes infinite number of blades and hence it further assumes that the forces acting on the rotor are distributed over the complete rotor disc surface. This means that all fluid particles passing through the rotor disk at a particular radial position would experience the same loss in axial momentum [9]. In reality, a wind turbine has a finite number of blades. As a result, flow slippage occurs at the tip of the blades from the pressure side to suction side of the blade due to pressure difference. This flow slippage is responsible for generating vortices at the tip region [15]. The flow slippage reduces the forces as well as the power production capacity throughout the length of the blade and particularly at the tip region. This effect is known as the tip loss effect [12].

BEMT-CFD model does not capture the effect of tip vortices and therefore it has two major shortcomings: it over predicts the performance and it generates unrealistic flow field. In Simple BEMT, the tip loss effect can be introduced via some empirical tip loss factor. An example of such a tip loss correction factor is the Prandtl tip loss factor. The implementation of the Prandtl tip loss factor reduces the forces acting throughout the length of the turbine blade. The reduction in the force is higher near the tip where the tip vortices have a pronounced effect [12]. When the Prandtl tip loss factor is applied to the BEMT-CFD, it not only reduces the forces exerted by the fluid on the blade, but it also reduces the reactive forces exerted by the blade on the fluid. As a result, the fluid passes through the turbine with little momentum change and the induced velocities predicted near the tip region are very low. Hence, the effect of the tip vortices is still not captured in the CFD-BEMT with the Prandtl tip loss model and the flow field prediction is still unrealistic. Further, due to unrealistic flow field prediction, the performance prediction is also not correct. This is not a problem with the BEMT with Prandtl tip loss model because the flow field is not simulated and incorporation of the tip loss model improves the performance prediction significantly as compared to the simple BEMT [7].

For the simulation of wind farms, an accurate prediction of downstream flow field of a wind turbine is as necessary as the accurate performance prediction of the turbine. This is because the accurate performance prediction of a downstream wind turbine is very much dependent on the downstream flow field generated by an upstream wind turbine. Hence the CFD-BEMT models, with and without tip loss correction factor, are not suitable for the simulation of wind farms and there is a need to develop more sophisticated CFD models which are capable of accurately predicting both the performance as well as the downstream flow field of a wind turbine.

Based on the motivations mentioned, the purpose of this thesis is to develop a more sophisticated CFD model, as compared to CFD-BEMT model, which is capable of accurately predicting both the performance of a turbine as well as the flow field. In this master thesis, three different CFD models are developed by combining the BEMT with the LLT and coupling them to a simple actuator disc concept in CFD. The models differ in the way of combining the LLT with the existing BEMT-CFD model. These models are termed as

the enhanced actuator disc models in this master thesis. Two research questions have to be answered by this thesis, which are:

1. Are the developed enhanced actuator disc models capable of accurately predicting the performance of a wind turbine as well as the flow field characteristics?
2. What is the effect of an upstream wind turbine on the performance of a downstream wind turbine using different CFD models?

1.3 Scope of thesis

At Stuttgart Wind Energy (SWE), CFD-BEMT model using actuator disc concept, with and without the Prandtl tip loss factor, was already incorporated in the ANSYS-CFX code before the start of this master thesis. The BEMT was coupled to the ANSYS-CFX using a FORTRAN code. The scope of this master thesis is specified as follows:

1. Incorporate the LLT to the already existing CFD-BEMT model of SWE, using three different approaches as explained later in chapter 3, to develop enhanced actuator disc models for CFD. Like the BEMT, the LLT is applied and combined with the BEMT using a FORTRAN code. The FORTRAN code is called by ANSYS-CFX as a user subroutine.
2. Perform CFD simulations for a single turbine using the three newly developed enhanced actuator disc models as well as using the older CFD-BEMT actuator disc models, with and without the Prandt tip loss factor. Compare the results with each other as well as with the reference results obtained from the FAST V8 code and the LLT IST code. Specifically:
    a. Variation of performance, power coefficient and thrust coefficient, with tip speed ratio.
    b. Variation of local flow field parameters, angle of attack, coefficient of drag, axial induction factor and tangential induction factor, with the radial position along the length of blade.
    c. Axial velocity field upstream and downstream of the turbine.
    d. Tangential velocity field downstream of the turbine.
    e. Turbulence kinetic energy in the flow field.
3. Perform CFD simulations for two turbines in a row using the three newly developed enhanced actuator disc models as well as the older CFD-BEMT actuator disc models, with and without the Prandtl tip loss factor. For two turbines in a row case, the results will only be compared to each other since no reference results are available either experimentally or from any commercial code. The following results will be compared with each other:
    a. Variation of the power of downstream wind turbine with tip speed ratio of upstream wind turbine. Here only the tip speed ratio of upstream turbine is changed while the tip speed ratio of downstream turbine is always kept the same for all simulations so that the only effect on the power of downstream wind turbine is due to the tip speed ratio of upstream wind turbine.

b. Variation of the thrust of downstream wind turbine with tip speed ratio of upstream wind turbine. Here only the tip speed ratio of upstream wind turbine is changed while the tip speed ratio of downstream wind turbine is always kept the same for all simulations so that the only effect on the thrust of downstream wind turbine is due to the tip speed ratio of upstream wind turbine.

CHAPTER 2: MODELS FOR WIND TURBINE ANALYSIS

2.1 Basics

A wind turbine is a device that extracts some of the kinetic energy from the wind. This extracted energy may be used to generate electricity. As a result of this extraction of kinetic energy from the wind, the wind slows down gradually from far upstream to far downstream. In steady axisymmetric flow through the turbine rotor disc, the portion of the air passing through the turbine constitutes a stream tube of circular cross section. No flow occurs across the boundary of stream tube. As the air slows down and it does not compress, the diameter of the stream tube increases by mass conservation. Since no energy is extracted until the air reaches the turbine, according to Bernoulli's Equation, the static pressure of the air must rise [3].

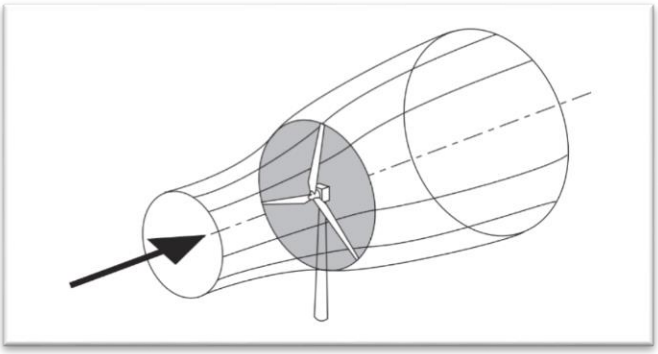

Figure 1: The energy extracting stream-tube of a wind turbine [3]

As the air passes through the turbine rotor, its pressure decreases suddenly in a step to below atmospheric level. The air then moves at the downstream side of the turbine with reduced velocity and reduced pressure

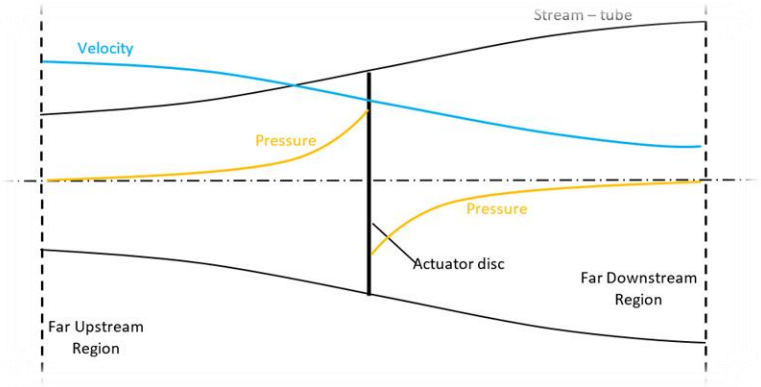

Figure 2: Static pressure and kinetic energy of air between far upstream and far downstream of the wind turbine

until at far downstream, where the pressure again increases to atmospheric pressure to attain equilibrium. Since no energy is added or extracted downstream of the rotor disc, the increase in pressure occurs on the expense of kinetic energy [3].

2.2 Blade Element Momentum Theory (BEMT)

The blade element momentum theory is a combination of the momentum theory and the blade element (BE) theory [12].

2.2.1 Momentum Theory

The aerodynamic behavior of wind turbines can be analyzed without considering any specific turbine design and just by considering the energy extraction process. The simplest device to accomplish this task is called actuator disc in which the turbine rotor with finite number of blades is replaced by a circular disc through which the air can flow [9].

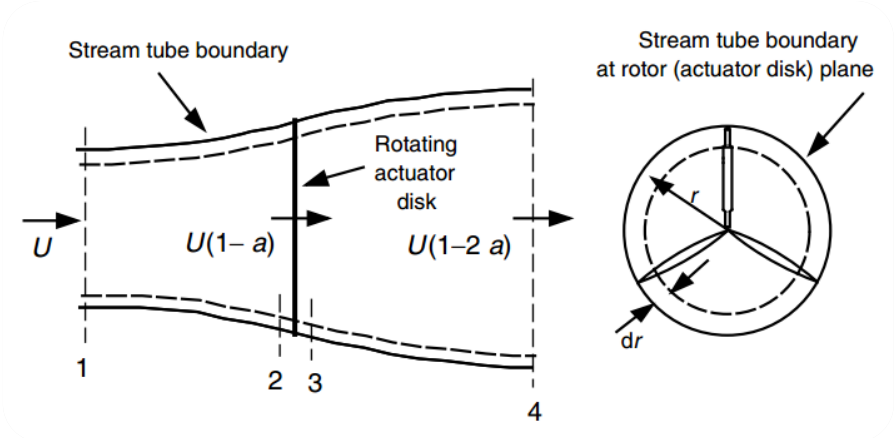

Figure 3: Geometry for rotor analysis

Momentum theory is one of the approaches used to determine the performance of the actuator disc. This analysis is based on the conservation of linear and angular momentum, conservation of mass and conservation of energy. The fluid flow exerts an axial force (thrust) as well as a torque on the turbine rotor. The analysis assumes a control volume in which the boundaries of the control volume are the surfaces of annular stream tube and two cross sections at the start and end of stream tube. Flow can only pass through the end cross sections and no flow is allowed to cross the surfaces of the stream tube into adjacent stream tubes [12].

The detailed analysis can be found in [12]. Here only the important and relevant formulas are given together with brief and relevant description.

The wind velocity of the undisturbed air is represented by U. U_1 , U_2, U_3, and U_4, represent the velocities of air at sections 1,2,3 and 4 in Figure 3.

The wind velocity at the rotor plane, using this simple model, is the average of the upstream and downstream wind speeds.

$$U_2 = \frac{U_1 + U_4}{2} \tag{1}$$

The axial induction factor is, a, is defined as

$$a = \frac{U - U_2}{U} \tag{2}$$

The quantity Ua often referred to as the induced velocity at the rotor. The velocity of the wind at the rotor is a combination of the free stream velocity and the induced wind velocity.

An angular induction factor, b, is defined as:

$$b = \frac{\omega}{2\Omega} \tag{3}$$

Where ω is the angular velocity of the flow stream imparted by the wind turbine and Ω is the angular velocity of the wind turbine.

The induced velocity at the rotor consists of not only the axial component, Ua, but also a component in the rotor plane, $r\Omega b$.

The expression for the axial force, A, exerted by the fluid on a differential element is given by:

$$dA = 4a(1 - a)\rho U^2 \pi r dr \tag{4}$$

where ρ is the density of the air.

The tip speed ratio, λ, defined as the ratio of the blade tip speed to the free stream wind speed, is given by:

$$\lambda = \frac{\Omega R}{U} \tag{5}$$

where R is the tip radius of wind turbine.

The local speed ratio is the ratio of the rotor speed at some intermediate radius, r, to the wind speed:

$$\lambda_r = \frac{\Omega r}{U} \tag{6}$$

The torque, Q, on a differential element is given by:

$$dQ = 4b(1 - a)\rho U \pi r^3 \Omega dr \tag{7}$$

2.2.2 Blade Element Theory

In the BE theory, the forces on the blades of a wind turbine can also be expressed as a function of the lift and drag coefficients and the angle of attack. For this analysis, the blade is assumed to be divided into a number of radial elements [12].

According to the theory of aerodynamics, lift and drag forces are perpendicular and parallel respectively to relative wind. The relative wind is the vector sum of the wind velocity at the rotor, $U(1 - a)$, and the wind velocity due to rotation of the blade, $\Omega r(1 + b)$ [12].

Figure 4 shows the relationships between the various angles, velocities and forces at a blade section. Here, ψ is the section pitch angle, which is the angle between the chord line and the plane of rotation; α is the angle of attack, which is the angle between the chord line and relative velocity of wind; ϕ is the undisturbed flow inclination angle; φ is the induced flow inclination angle; dL is the incremental lift force; dD is the incremental drag force; dA is the incremental axial force (normal to the plane of rotation); and dT is the incremental tangential force (parallel to the plane of rotation). This is the force is responsible for creating useful torque. Finally, U_{rel} is the relative wind velocity [12].

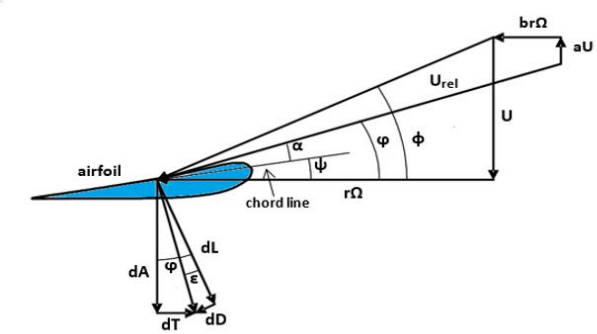

Figure 4: Velocity triangle at a blade section

Here again, only the relevant and most important relations are given for the BE theory. The details can be found in [12].

The induced flow inclination angle is given by:

$$\tan\varphi = \frac{U(1-a)}{\Omega r(1+b)} \tag{8}$$

The total axial force on the section at a distance, r, from the center is:

$$dA = \frac{1}{2}B\rho U_{rel}^2(C_L\cos\varphi + C_D\sin\varphi)cdr \tag{9}$$

where B is the number of blades, C_L is the lift coefficient, C_D is the drag coefficient and U_{rel} is the relative velocity of wind.

The differential torque due to the tangential force acting at a distance, *r,* from the center is given by:

$$dQ = \frac{1}{2}B\rho U_{rel}^2(C_L\sin\varphi - C_D\cos\varphi)crdr \tag{10}$$

2.2.3 Blade Element Momentum Theory

BEMT is the combination of BE and momentum theories. In BEMT, axial force and torque from BE are forced to match axial force and torque from momentum theory [12].

In the calculation of induction factors, *a* and *b*, accepted practice is to set C_D equal to zero (see Wilson and Lissaman, 1974). So, when the torque equations from momentum and blade element theory are equated (Equations (7) and (10)), with C_D= 0, one gets

$$\frac{b}{(1-a)} = \frac{\sigma' C_L}{(4\lambda_r \sin\varphi)} \tag{11}$$

Where σ' is the local solidity, defined by:

$$\sigma' = \frac{Bc}{2\pi r} \tag{12}$$

By equating the axial force equations from momentum and blade element theory (Equations (4) and (9)), one obtains:

$$\frac{a}{(1-a)} = \frac{\sigma' C_L \cos\varphi}{(4\sin^2\varphi)} \tag{13}$$

After some algebraic manipulations, these equations are solved iteratively to determine the flow conditions and forces at each blade section.

The power contribution from each annulus is

$$dP = \Omega dQ \tag{14}$$

The total power from the rotor is:

$$P = \int_{r_h}^{R} \Omega dQ \tag{15}$$

Where r_h is the hub radius.

2.2.4 Tip Loss: Effect on Power Coefficient of Number of Blades

Because the pressure on the upper side of a blade is lower than that on the lower side, air tends to flow around the tip from the lower to upper surface, reducing the lift and hence the power production near the tip. [12]. A number of methods have been suggested for including the effect of the tip loss. The most straightforward approach to use is one developed by Prandtl (see de Vries, 1979). According to this method, a correction factor, F, must be introduced into the previously discussed equations

$$F = \left(\frac{2}{\pi}\right)\cos^{-1}\left[exp\left(-\left\{\frac{(B/2)[1-(r/R)]}{(r/R)\sin\varphi}\right\}\right)\right] \tag{16}$$

Note that F is always between 0 and 1. This tip loss correction factor characterizes the reduction in the forces at a radius r along the blade that is due to the tip loss. Thus Equations (4) and (7) become:

$$dA = F4a(1-a)\rho U^2 \pi r dr \tag{17}$$

And

$$dQ = 4Fb(1-a)\rho U \pi r^3 \Omega dr \tag{18}$$

2.3 Lifting Line Theory (LLT)

In a wind turbine, vortices are generated at the tip region due to pressure difference between upper and lower surface of the blade. Tip vortices reduce the angle of attack relative to an idealized infinitely long 2D airfoil which in turn causes reduction in lift force.

The lift force on a wing is produced due to pressure differential between the lower and upper surfaces of the wing. The associated difference in flow speed above and below the wing section can be characterized as circulation (or vorticity). The induced circulation makes the flow to deflect downwards. This downward deflection is called as downwash [7]. According to circulation theory, see [1], the lift force of a wing of constant section and unit span is calculated as:

$$L = \rho U \Gamma \tag{19}$$

where Γ is the circulation.

Figure 5 shows that the geometric angle of attack α is composed of two further components; induced angle of attack α_i and the effective angle of attack α_e. The induced angle of attack is the angle of downward deflection resulting from induced downwash [11]. The induced angle of attack can be computed by:

$$\alpha_i = \tan^{-1} w/U \tag{20}$$

The effective angle of attack is given by:

$$\alpha_e = \alpha - \alpha_i \tag{21}$$

Wing tip vortices are explained in [15] and [1]. These wing tip vortices downstream of the wing induce an additional small downward component of air velocity in the neighborhood of the wing itself. This additional downward component, additional downwash (or additional induced velocity), varies across the length of a finite wing. The span wise component of air vector on the upper surface is directed from tip to hub, and on the lower surface the span wise component of velocity is directed from hub to tip. The physical effect of the resultant shear at the trailing edge is the development of a trailing vortex sheet which contains vorticity [7]. Prandtl's classical lifting line theory, as detailed in [15], describes this phenomenon in terms of an infinite number of horseshoe vortices distributed across the wing span, compounded towards the root of the span.

Prandtl's classical lifting line theory is an approach that uses this system of horse shoe vortices (bound wing vortices and trailing wing vortices) to determine the induced velocities and forces on the wing. According to the LLT, for a wing of finite length, α_e at the wing tip is constrained as the angle of attack at which lift force reduces to zero. This then influences the distribution of downwash across the span [7]. Hence when LLT is applied to wind turbines, it is capable of predicting the induced velocities generated by the horse shoe vortex system and further calculate the forces on the blades of the turbine.

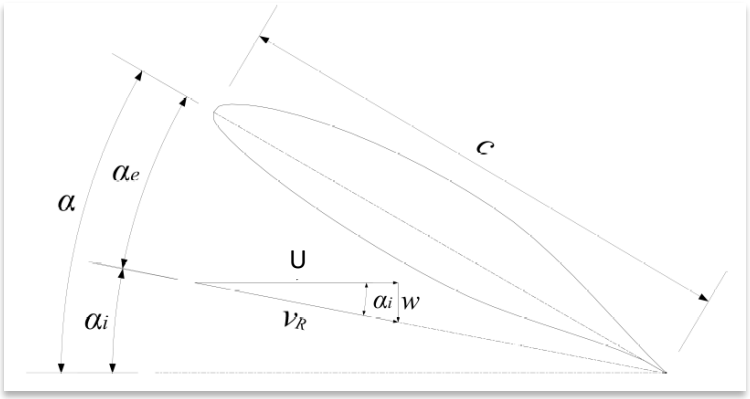

Figure 5: This diagram highlights the components required to define the induced angle of attack

The following Lifting line theory for the designing of turbine till the end of this section is taken from [4]. It is assumed that the turbine, having B number of blades, is subjected to a uniform axial airstream of velocity U. Flow is steady in the reference frame of turbine. Each turbine blade is assumed to be replaced by a radial line vortex having circulation strength $\Gamma(r)$ which varies along the radial line from the hub radius $r = r_h$ to the blade tip $r = R$.

The effect of turbine hub is incorporated by considering the potential flow disturbance by an approximate image method assuming an infinitely long cylinder of radius $r = r_h$. In this case, the lifting line circulation may be different from zero at the hub radius. At the tip, the circulation reduces to zero $\Gamma(R) = 0$. A trailing vortex sheet is emitted from each lifting line. It is assumed that the trailing vortices are helical in nature with constant radius and pitch in the stream wise direction.

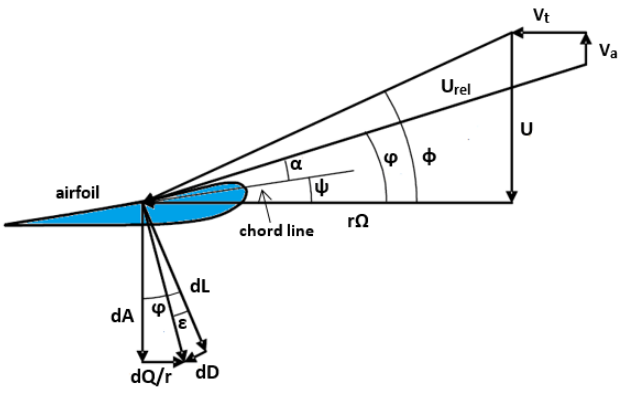

Figure 6: Velocity triangle at blade section

The velocity triangle for a blade section at radius r is shown in Figure 6. The axial and tangential induced velocities at the lifting line may be written as:

$$\nu_{a,t}(r) = \frac{1}{4\pi}\int_{r_h}^{R}\frac{d\Gamma}{dr'}\frac{i_{a,t}}{r-r'}dr \tag{22}$$

where

$$i_{a,t} = \left(\frac{r}{r'},\frac{r'}{r_h},\varphi_v,B\right) = i_{a,t}\left(\frac{r}{r'},\varphi_v,B\right) - i_{a,t}\left(\frac{r}{r'^{(im)}},\varphi_v^{im},B\right) \tag{23}$$

are axial and tangential induction factors due to a set of B semi-infinite helical vortices of radius *r'* and pitch angle φ_v, which are modified to take into account the velocity induced by approximate image vortices generated due to presence of infinitely long cylinder of radius r_h. The approximate image vortices are semi-infinite helical vortices and with radius $r'^{(im)} = r_h^2/r'$ and the pitch angle satisfying $tan\phi_v^{(im)} = (r'/r'^{(im)})tan\phi_v$. $i_{a,t}\ (r/r', \phi_v, B)$ are the usual axial and tangential induction factors for helicoidal vortices in the lifting line theory [13]. For their evaluation asymptotic formulas of Morgan and Wrench (1965) can be used. In the moderately loaded theory, we can determined the induced flow inclination angle as:

$$\varphi_v(r) = \varphi(r) = \tan^{-1}\frac{U-\nu_a}{\Omega r+\nu_t} \tag{24}$$

Kutta-Joukowski law is used to calculate the inviscid forces on the lifting line. The viscous effects on the axial force and torque can be included by introducing the drag to lift ratio $\varepsilon = dD/dL = C_D/C_L$ of the blade section forces, see Figure 6. The axial force and the torque on the rotor are obtained by integration along the radius and summing on the number of blades:

$$A = \rho B\int_{r_h}^{R}(\Omega r+\nu_t)(1+\varepsilon\tan\varphi)\Gamma(r)dr \tag{25}$$

$$Q = \rho B\int_{r_h}^{R}(U-\nu_a)(1-\varepsilon\cot\varphi)\Gamma(r)rdr \tag{26}$$

Where ρ is the fluid density

Blade section lift and drag coefficients are defined by

$$C_L = \frac{dL/dr}{1/2\rho U_{rel}^2 c}, \qquad C_D = \frac{dD/dr}{1/2\rho U_{rel}^2 c} \tag{27}$$

where U_{rel} is the relative velocity of wind and *c is* the chord of the blade section. Using Kutta-Joukowski law the coefficient of lift can be calculated as

$$C_L = \frac{2\Gamma}{U_{rel}c} \tag{28}$$

The section pitch angle is related to induced flow inclination angle by

$$\psi = \varphi - \alpha \tag{29}$$

Where α is the section angle of attack at the corresponding lift coefficient (Figure 6).The lift and drag coefficients of the blade section are assumed to be a function of the angle of attack and of the section Reynolds number, $Re.$

Dimensionless quantities are introduced by using the turbine tip radius, R, as reference length and the incoming free stream air velocity, U, as reference velocity. The turbine thrust and power coefficients are defined by

$$\mathrm{C_T} = \frac{A}{\frac{1}{2}\rho U^2 \pi R^2} \tag{30}$$

$$\mathrm{C_P} = \frac{P}{\frac{1}{2}\rho U^3 \pi R^2} = \frac{\Omega Q}{\frac{1}{2}\rho U^3 \pi R^2} \tag{31}$$

Which are functions of the turbine tip-speed-ratio $\lambda = (\Omega R)/U$ and the turbine Reynolds number.

CHAPTER 3: CFD-MODELS

In this chapter, the description of CFD models used in this thesis is provided. First, the governing equations of CFD are discussed. Then the already exiting CFD-BEMT model and newly developed enhanced actuator disc models are discussed.

3.1 The RANS equations

Simulations were performed using ANSYS-CFX with the Reynolds-Averaged Navier-Stokes (RANS) equations, which are obtained by averaging the fluctuating quantities in the original transport equations. In the following steady-state RANS equations, the bar is dropped for averaged quantities, except for products of fluctuating quantities.

Continuity equation is given as:

$$\frac{\partial}{\partial x_j}\rho(U_j) = 0 \tag{32}$$

Momentum equation is given as:

$$\frac{\partial}{\partial x_j}\rho(U_i U_j) = -\frac{\partial p}{\partial x_i} + \frac{\partial}{\partial x_j}(\tau_{ij} - \rho\overline{U_i U_j}) + S_i \tag{33}$$

where ρ is the density, U_i (i = u, v, w) is the averaged velocity, $\mathrm{x_i}$ ($\mathrm{i} = \mathrm{x, y, z}$) is the position, p is the mean pressure, τ is the molecular stress tensor, $\rho\overline{U_i U_j}$ are the Reynolds stresses, and S_i are additional source terms in the $\mathrm{i} = \mathrm{x, y, z}$ momentum equations. The Reynolds stresses are calculated from the k-ω SST model.

3.2 CFD-BEMT model

This method is based on the solution of RANS equations in combinations in combination with the BEMT. When an airfoil moves through air, aerodynamic force is exerted on the airfoil. This force can be resolved into two mutually perpendicular components, the lift force, L, and the drag force, D, defined as follows.

$$L = 0.5\rho U_{rel}^2 A_r C_L \tag{34}$$

$$D = 0.5\rho U_{rel}^2 A_r C_D \tag{35}$$

where ρ is the density of air, U_{rel} is the relative velocity of air, A_r is the area of the object, C_L is the lift coefficient and C_D is the drag coefficient. The lift and drag coefficients are dependent on the angle of attack, α, the Reynolds number, Re, and the geometric properties of airfoil.

In the BEMT, the effect of multiple blades is averaged over one complete rotation. In the CFD-BEMT model, the effect of blade on the fluid is introduced through momentum source terms in Navier-Stokes equations (see Equation (33)).

BEMT discretize the blade in a number of elements as shown in Figure 7. The forces on each blade section are as shown again in the Figure 8.

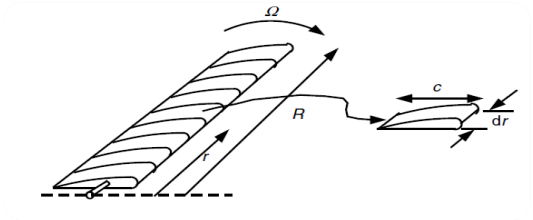

Figure 7: Schematics of blade elements

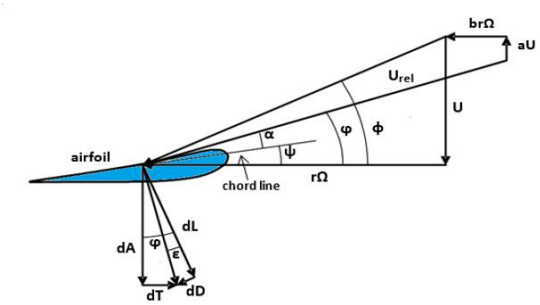

Figure 8: Velocity triangle of a blade section

The induced flow inclination angle is defined as:

$$\varphi = \tan^{-1}\frac{U(1-a)}{\Omega r(1+b)} \tag{36}$$

Relative wind velocity is given by:

$$U_{rel}^2 = [U(1-a)]^2 + [\Omega r(1+b)]^2 \tag{37}$$

Where U is undisturbed wind velocity, Ω is angular velocity of turbine, r is the radius of blade element, a is axial induction factor and b is tangential induction factor. Here it is important to mention that in CFD-BEMT model, a and b are calculated directly from the RANS calculations.

The lift force and drag force on a blade element are given by:

$$dL = 0.5\rho U_{rel}^2 C_L c dr \tag{38}$$

$$dD = 0.5\rho U_{rel}^2 C_D c dr \tag{39}$$

where c is the chord length.

Using Figure 8, lift force and drag force are related to axial force and tangential force as follows

$$dA = dL\cos\varphi + dD\sin\varphi \tag{40}$$

$$dT = dL\sin\varphi - dD\cos\varphi \tag{41}$$

Substituting Equations (38) and (39) into Equations (40) and (41) gives:

$$dA = 0.5\rho U_{rel}^2 cdr(C_L \cos\varphi + C_D \sin\varphi) \quad (42)$$

$$dT = 0.5\rho U_{rel}^2 cdr(C_L \sin\varphi - C_D \cos\varphi) \quad (43)$$

Which when converted to force per unit will give the axial and tangential momentum source terms, ST_{ax} and ST_{tan} to be incorporated in Navier-Stokes Equations.

$$ST_{ax} = \frac{BdA}{2\pi r\Delta x dr} \quad (44)$$

$$ST_{tan} = \frac{BdT}{2\pi r\Delta x dr} \quad (45)$$

where B is the number of blades and Δx is the thickness of the actuator disc

When the Prandtl Tip loss correction is used, Equations (44) and (45) becomes

$$ST_{ax} = \frac{BFdA}{2\pi r\Delta x dr} \quad (46)$$

$$ST_{tan} = \frac{BFdT}{2\pi r\Delta x dr} \quad (47)$$

, Where F is the Prandtl tip loss factor given as

$$F = \left(\frac{2}{\pi}\right)\cos^{-1}\left[exp\left(-\left\{\frac{(B/2)[1-(r/R)]}{(r/R)\sin\varphi}\right\}\right)\right] \quad (48)$$

3.3 Enhanced actuator disc models (CFD-BEMT+LLT Models)

To address the issue of simultaneously improving performance prediction and flow field, in this model the BEMT and the LLT are combined. The LLT has the capability of taking tip vortices into account and accurately predicting the local flow field. Since the tip vortices has strong impact only near the tip region, the LLT is coupled with the BEMT in the last 10% of the blade length at the tip side. From now on, this region will be referred as the *BEMT+LLT* region. In the remaining 90% of the blade length starting from center of turbine, simple BEMT is used. From now on, this region will be referred as *BEMT* region. This is shown in Figure 9.

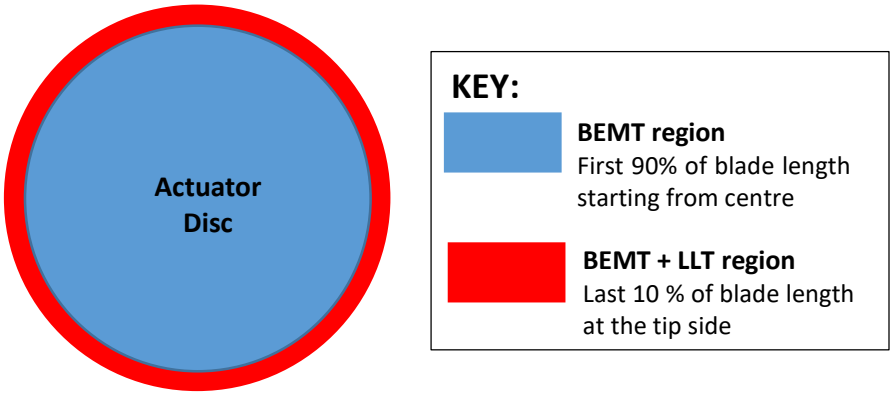

Figure 9: Regions of actuator disc for CFD-BEMT+LLT model

3.3.1 BEMT region

In the CFD-BEMT model discussed earlier, the BEMT was incorporated to CFD by calculating and applying axial and tangential momentum source terms derived using the BEMT, as shown in Equations (36) to (45). In the CFD-BEMT+LLT models, the same formulations and procedure is used for the CFD-BEMT region as in that region only the BEMT is coupled with CFD.

3.3.2 BEMT+LLT region

In the BEMT+LLT region, both for axial and tangential directions, two momentum source terms are calculated. They will onwards be referred as simple momentum source terms and additional momentum source terms. These two are combined to give cumulative momentum source terms for the BEMT+LLT region.

3.3.2.1 Simple Momentum Source Terms:

Tip vortices generate additional induced velocities. These additional induced velocities reduce the forces on the blade particularly in the tip region. The LLT captures the effect of the tip vortices on the induced velocities. Simple momentum source terms will impart the effect of reactive forces of the turbine blade on the fluid. In the calculation of simple momentum source terms for the BEMT+LLT region, induced velocities calculated from the LLT are used in the CFD-BEMT model (discussed earlier) in contrast to axial and tangential induction factors obtained from the RANS calculations of the current flow field iteration. The result is that, the forces on the blades and hence the momentum source terms are reduced as compared to the simple CFD-BEMT model.

To calculate simple momentum source terms, LLT is used to calculate axial and tangential induced velocities, v_a and v_t, in the BEMT+LLT region. These induced velocities are used to find the induced flow inclination angle as below:

$$\varphi = \tan^{-1}\frac{U - v_a}{\Omega r + v_t} \tag{49}$$

The relative velocity of the wind is calculated as:

$$U_{rel}^2 = [U - v_a]^2 + [\Omega r + v_t]^2 \tag{50}$$

After finding the flow inclination angle and relative velocity using induced velocities calculated from the LLT, simple momentum source terms are calculated using the same formulations and procedure as that of CFD-BEMT model from Equation (38) to (45).

3.3.2.2 Additional momentum source terms.

Additional momentum source terms represent the effect of the tip vortices on the fluid in terms of induced velocities. The induced velocities calculated by the LLT contain the effect of the tip vortices. The idea used to calculate the additional momentum source terms is that to calculate the difference in induced velocities from the LLT and the RANS calculations and transform that difference in velocity into a force. Three different

approaches, Method 1, Method 2 and Method 3, are used to transform the difference in induced velocity to the force.

3.3.2.2.1 Method 1 (M1)

This method is taken from Edmunds et al [7]. According to this method, the additional reactive force, dF_v, at the tip required to produce zero lift condition at the tip is given by

$$dF_v = 0.5\rho w_a^2 c dr \tag{51}$$

Where w_a is the additional downwash (additional induced velocity) required to achieve zero lift condition at the tip. In Method 1 of calculating additional momentum source terms, additional axial and tangential induced velocities are calculated which are required to bring the induced velocities from the RANS calculations to the induced velocities from the LLT. These additional induced velocities are calculated by taking the difference of induced velocities from the LLT and the RANS calculations. This difference in the induced velocities is used to calculate the additional reactive forces in the axial and tangential direction, dF_A and dF_T , separately as follows:

$$dF_A = 0.5\rho\left(v_{a_{LLT}} - v_{a_{RS}}\right)^2 c dr \tag{52}$$

$$dF_T = 0.5\rho\left(v_{t_{LLT}} - v_{t_{RS}}\right)^2 c dr \tag{53}$$

where $v_{a_{LLT}}$ and $v_{t_{LLT}}$ are the axial and tangential induced velocity from the LLT and $v_{a_{RS}}$ and $v_{t_{RS}}$ are the axial and tangential induced velocities from RANS calculations. The additional reactive force when converted to force per unit volume gives the additional momentum source terms as follows

$$AST_{ax} = \frac{BdF_A}{2\pi r \Delta x dr} = \frac{B\rho\left(v_{a_{LLT}} - v_{a_{RS}}\right)^2 c}{4\pi r \Delta x} \tag{54}$$

$$AST_{ax} = \frac{BdF_t}{2\pi r \Delta x dr} = \frac{B\rho\left(v_{t_{LLT}} - v_{t_{RS}}\right)^2 c}{4\pi r \Delta x} \tag{55}$$

The additional momentum source terms calculated from this method are considerably smaller than those calculated from M2 and M3.

3.3.2.2.2 Method 2 (M2)

This method is based on momentum balance and uses Newton's second Law of motion. Difference in induced velocities from the LLT and the RANS calculations is obtained. This difference is used to calculate the rate of change of momentum, required to produce this change of velocity, which is equivalent to force. Axial and tangential forces, dF_A and dF_T are calculated as

$$\mathrm{dF_A} = \left(\rho\left(U - v_{a_{RS}}\right)dA_r\right) * \left(v_{a_{LLT}} - v_{a_{RS}}\right) \tag{56}$$

$$\mathrm{dF}_T = \left(\rho\left(U - v_{a_{RS}}\right)dA_r\right) * \left(v_{t_{LLT}} - v_{t_{RS}}\right) \tag{57}$$

where dA_r is the cross section area of differential control volume, $v_{a_{LLT}}$ and $v_{t_{LLT}}$ are the axial and tangential induced velocity from the LLT and $v_{a_{RS}}$ and $v_{t_{RS}}$ are the axial and tangential induced velocities from RANS calculations. Additional momentum source terms are calculated by finding the force per unit of volume. The procedure is applied for both axial and tangential source terms. The axial and tangential source terms, AST_{ax} and AST_{tan}, for this method are given as

$$AST_{ax} = \frac{dF_A}{dA_r \Delta x} = \frac{\rho\left(U - v_{a_{RS}}\right)(v_{a_{LLT}} - v_{a_{RS}})}{\Delta x} \tag{58}$$

$$AST_{tan} = \frac{dF_T}{dA_r \Delta x} = \frac{\rho\left(U - v_{a_{RS}}\right)(v_{t_{LLT}} - v_{t_{RS}})}{\Delta x} \tag{59}$$

The source terms calculated from this method are higher than M1 and lower than M3.

3.3.2.2.3 Method 3 (M3)

This method is similar to Method 2. The only difference is that the induced velocities from the flow field are assumed to be zero, which holds strictly at the tip. Hence, difference in induced velocities from LLT and flow field reduces to absolute value of induced velocities from LLT. This method is not physical but is used to increase the source terms and observe the effects of increased additional momentum source terms. The axial and tangential source terms for this method are given as

$$AST_{ax} = \frac{dF_A}{dA_r \Delta x} = \frac{\rho\left(U - v_{a_{RS}}\right)(v_{a_{LLT}})}{\Delta x} \tag{60}$$

$$AST_{tan} = \frac{dF_T}{dA_r \Delta x} = \frac{\rho\left(U - v_{a_{RS}}\right)(v_{t_{LLT}})}{\Delta x} \tag{61}$$

3.4 Calculation of power coefficient (C_P) and thrust coefficient (C_T)

$$C_P = \frac{\omega Q}{\frac{1}{2}\rho U^3 A_s} = \sum \frac{\omega \delta Q}{\frac{1}{2}\rho U_3 A_s} \tag{62}$$

$$C_T = \frac{A}{\frac{1}{2}\rho U^2 A_s} = \sum \frac{\delta A}{\frac{1}{2}\rho U^2 A_s} \tag{63}$$

Where A_s is the rotor swept area which is corresponding to the sectional area of the disc, Q is the torque obtained from the product of the radius (r) and the tangential force (T) in the BEM-CFD simulation, and A is the axial force acting on the turbine which is equivalent to the thrust force. Thus, the equivalent C_P and C_T are calculated by summation over each element with width dr.

CHAPTER 4: COMPUTATIONAL CODES

In this master thesis, three computational codes are used; ANSYS-CFX. FAST V8 and LLT IST code. The CFD simulations are performed in ANSYS-CFX. Brief details of these codes are given below.

4.1 ANSYS-CFX

4.1.1 Introduction to ANSYS-CFX

ANSYS CFX is a general purpose software suit that uses Computational Fluid Dynamics (CFD) to solve the fluid problems. ANSYS combines an advanced solver with powerful preprocessing and post processing capabilities. ANSYS-CFX is based on the control volume fixed in space fluid model. [2].

4.1.2 The Structure of ANSYS-CFX

ANSYS-CFX consists of four software modules:

4.1.2.1 CFX-Pre

CFX-Pre is used to define simulations. Multiple meshes may be imported, allowing each section of complex geometries to use the most appropriate mesh. Analyses, which consist of flow physics, boundary conditions, initial values, and solver parameters, are also specified. A full range of boundary conditions, including inlets, outlets and openings, together with boundary conditions for heat transfer models and periodicity, are all available in ANSYS-CFX through CFX-Pre [2].

4.1.2.2 CFX-Solver

CFX-Solver solves all the solution variables for the simulation for the problem specification generated in CFX-Pre. One of the most important features of ANSYS-CFX is its use of a coupled solver, in which all the hydrodynamic equations are solved as a single system which results in a faster converged solution as compared to traditional segregated solver [2].

4.1.2.3 CFX-Solver Manager

The CFX-Solver Manager module provides greater control to the management of the CFD task. Its major functions are to specify the input files to the CFX-Solver, Start/stop the CFX-Solver, monitor the progress of the solution and set up the CFX-Solver for a parallel calculation [2].

4.1.2.4 CFD-Post

CFD-Post provides interactive post processing graphics tools to examine the ANSYS CFX simulation results. Important features include quantitative post-processing, report generation, user-defined variables, generation of a variety of graphical objects where visibility, transparency, color, and line/face rendering can be controlled and power syntax to allow fully programmable session files [2].

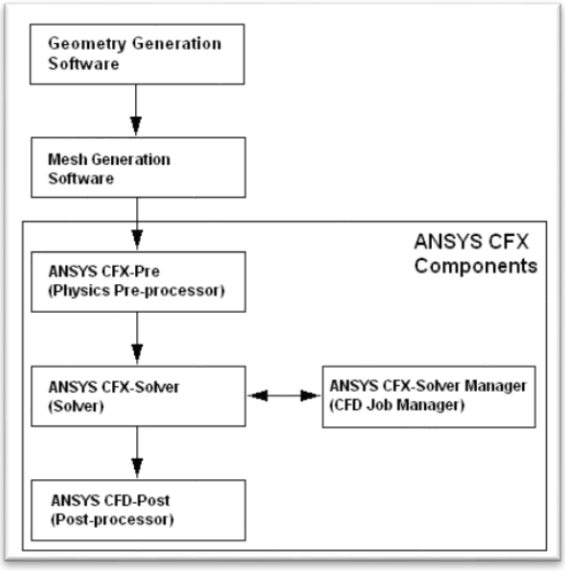

Figure 10: structure of ANSYS-CFX

4.2 FAST V8

The FAST (Fatigue, Aerodynamics, Structures, and Turbulence) is an open source computer aided engineering (CAE) tool developed by NREL (National Renewable Energy Laboratory). It is a comprehensive multiphysics engineering software tool used to design and analyze horizontal axis wind turbines. The novel FAST v8 contains modules for aerodynamics (AeroDyn); hydrodynamics (HydroDyn); control and electrical drive dynamics (ServoDyn); rotor, drivetrain, nacelle, tower, and platform structural dynamics (ElastoDyn); multimember substructure structural dynamics (SubDyn); mooring statics and dynamics (MAP); and ice loads (IceFloe) [5].

AeroDyn is a set of routines used in conjunction with an aeroelastic simulation code to predict the aerodynamics of horizontal axis wind turbines. AeroDyn has the capability to determine the aerodynamics characteristics of wind turbines using two types of models; the BEMT and the generalized dynamic-wake theory. For this master thesis, AeroDyn is used to obtain some reference results using BEMT model, both with and without the Prandtl tip loss correction [14].

4.3 LLT IST code

LLT IST code is developed in Instituto Superior Técnico, Portugal. This code uses the LLT to determine the aerodynamic characteristics of a wind turbine. The code is based on the induction factor method of Lerbs (1952) combined with a vortex-lattice method for the discretization of the lifting line (Falcão de Campos, 2007, Baltazar et al, 2011). The implementation of the induction factors follows the formulation of Morgan and Wrench (1965). The local flow field parameters, which include axial and tangential induced velocities, α, and C_D, obtained from CFD simulations are compared with those obtained from LLT IST code. Further, the LLT is applied in the CFD simulations via a FORTRAN subroutine. This subroutine is derived from the same LLT IST code.

CHAPTER 5: REFERENCE TURBINE FOR CFD SIMULATIONS

For this thesis, turbine specifications of "NREL offshore 5-MW baseline wind turbine" are used. The specifications of the turbine are developed by NREL of The U.S. Department of Energy (DOE) to support the concept studies for assessing offshore wind technology. This wind turbine is a conventional three-bladed upwind variable-speed variable blade-pitch-to-feather-controlled turbine. NREL has given the specifications for gross properties of turbine, blade structural properties, blade aerodynamic properties, hub and nacelle properties, drivetrain properties, tower properties and baseline control system properties [11]. Here only gross properties of turbine and aerodynamic properties of turbine will be provided as only these properties are relevant to this thesis.

5.1 Gross properties of turbine

The gross properties of NREL offshore 5-MW baseline wind turbine are given in Table 1.

Rating	5 MW
Rotor Orientation, Configuration	Upwind, 3 Blades
Control	Variable Speed, Collective Pitch
Drivetrain	High Speed, Multiple-Stage Gearbox
Rotor, Hub Diameter	126 m, 3 m
Hub Height	90 m
Cut-In, Rated, Cut-Out Wind Speed	3 m/s, 11.4 m/s, 25 m/s
Cut-In, Rated Rotor Speed	6.9 rpm, 12.1 rpm
Rated Tip Speed	80 m/s
Overhang, Shaft Tilt, Precone	5 m, 5º, 2.5º
Rotor Mass	110,000 kg
Nacelle Mass	240,000 kg
Tower Mass	347,460 kg

Table 1: Gross properties of reference turbine [11]

5.2 Blade aerodynamic Properties

The aerodynamic properties of the turbine used in the CFD simulations are given in Table 2. The table shows pitch, chord and airfoil distribution along the blade. Eight airfoils are used for this turbine. The two innermost airfoils represent cylinders with drag coefficients of 0.50 and 0.35 and zero lift. The effect of hub is neglected by using both lift and drag coefficients equal to zero. The airfoil data (C_L and C_D against α) for all the airfoils used is given in [11]. Here it is important to note that in this thesis the original airfoil distribution provided by NREL is not used due to a mistake that was realized after the majority of the simulations were

conducted. The airfoils used in this thesis are same as provided by NREL but their distribution along the radial position is different as compared to the distribution provided by NREL. However, this does not affect the purpose of this thesis since the thesis is based on the comparison of results and all the analysis (CFD simulations as well as reference result from FAST V8 and LLT IST code) are done with the same airfoil distributions.

Radius	Pitch (˚)	chord(m)	Airfoil
0	13.308	3.542	Hub
1.5	13.308	3.542	Cylinder 1
4.2334	13.308	3.698006	Cylinder 1
6.9666	13.308	4.010494	Cylinder 2
9.7	13.308	4.323002	DU21_A17
11.75	13.308	4.557	DU21_A17
13.8	12.394	4.6045	DU25_A17
15.85	11.48	4.652	DU25_A17
17.9	10.821	4.555	DU25_A17
22	9.5865	4.3535	DU30_A17
26.1	8.403	4.128	DU35_A17
30.2	7.1695	3.8775	DU35_A17
34.3	5.9525	3.625	DU40_A17
38.4	4.7745	3.379	DU40_A17
42.5	3.6565	3.133	NACA64_A17
44.55	3.125	3.01	NACA64_A17
46.6	2.722	2.887	NACA64_A17
50.7	1.9225	2.641	NACA64_A17
54.8	1.128204	2.395001	NACA64_A17
57.5334	0.616491	2.199496	NACA64_A17
58.9	0.37	2.086	NACA64_A17
60.2666	0.238005	1.752512	NACA64_A17
61.6333	0.106	1.419	NACA64_A17
63	0.053	0.7095	NACA64_A17

Table 2: Aerodynamic properties of reference turbine

CHAPTER 6: ANSYS-CFX SIMULATION SETUP

6.1 Overview

In this section description of flow domain and simulation setup is given. Simulations are performed for single turbine case and two turbines in a row case. The flow domain used is 1500 X 600 X 600 m for single turbine

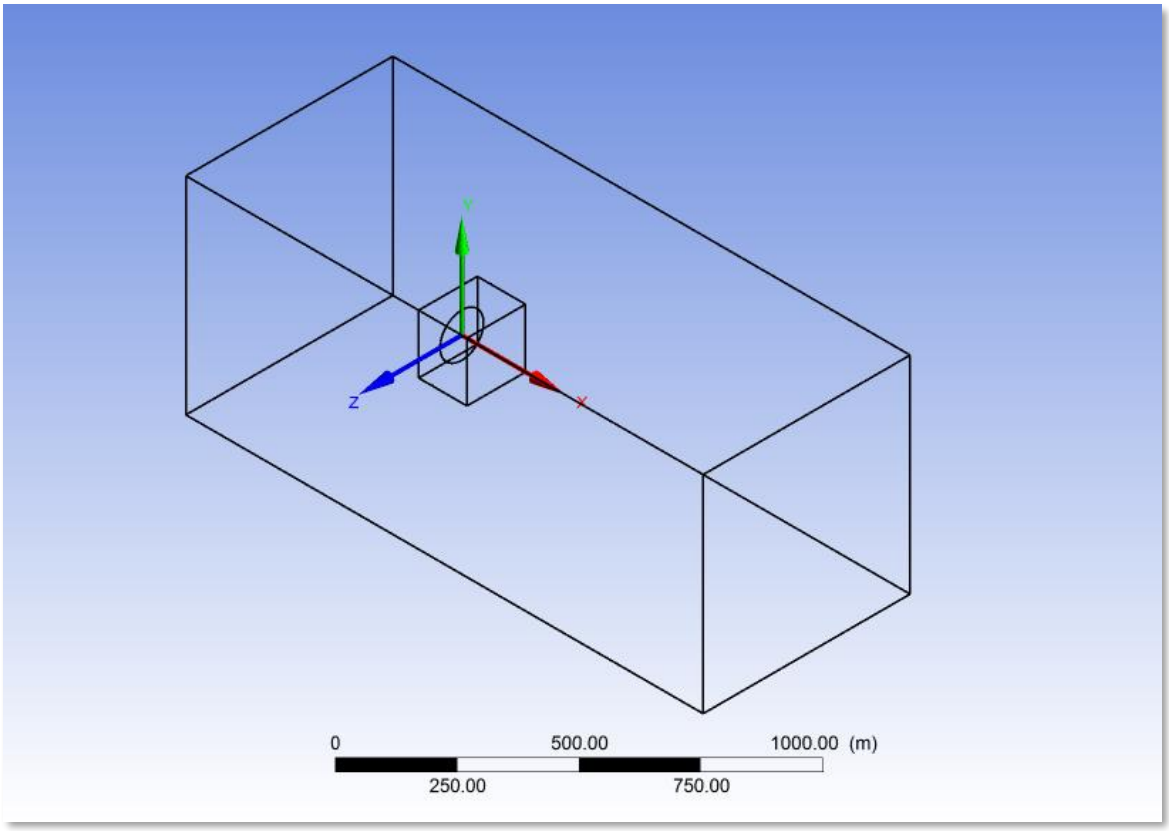

Figure 11: Isometric view of flow field setup with reference coordinate frame

case and 2350 X 600 X 600 m for two turbines in a row case. The flow domain is surrounded by six boundaries and contains three types of mesh regions. These boundaries and mesh regions will be explained in later sections. The actuator disc is built according to original dimensions i.e. on a scale of 1:1. In two turbines in a row case, the turbines are placed 849.5m apart. Figures 11 and 12 show the setup for the single turbine case in the ANSYS-CFX. Axial velocities are parallel to x-axis while tangential velocities are in planes parallel to yz-plane. The origin of the reference coordinate frame is at the center of turbine as shown in Figure 11. The fluid used in simulations is air at 25˚C. The magnitude of inlet velocity is set at 8 m/s for all the calculations.

6.2 Boundary Conditions

The flow domain has 6 boundaries which are named inlet, outlet, top, bottom and 2 sides. The characteristics of these boundaries are as follows.

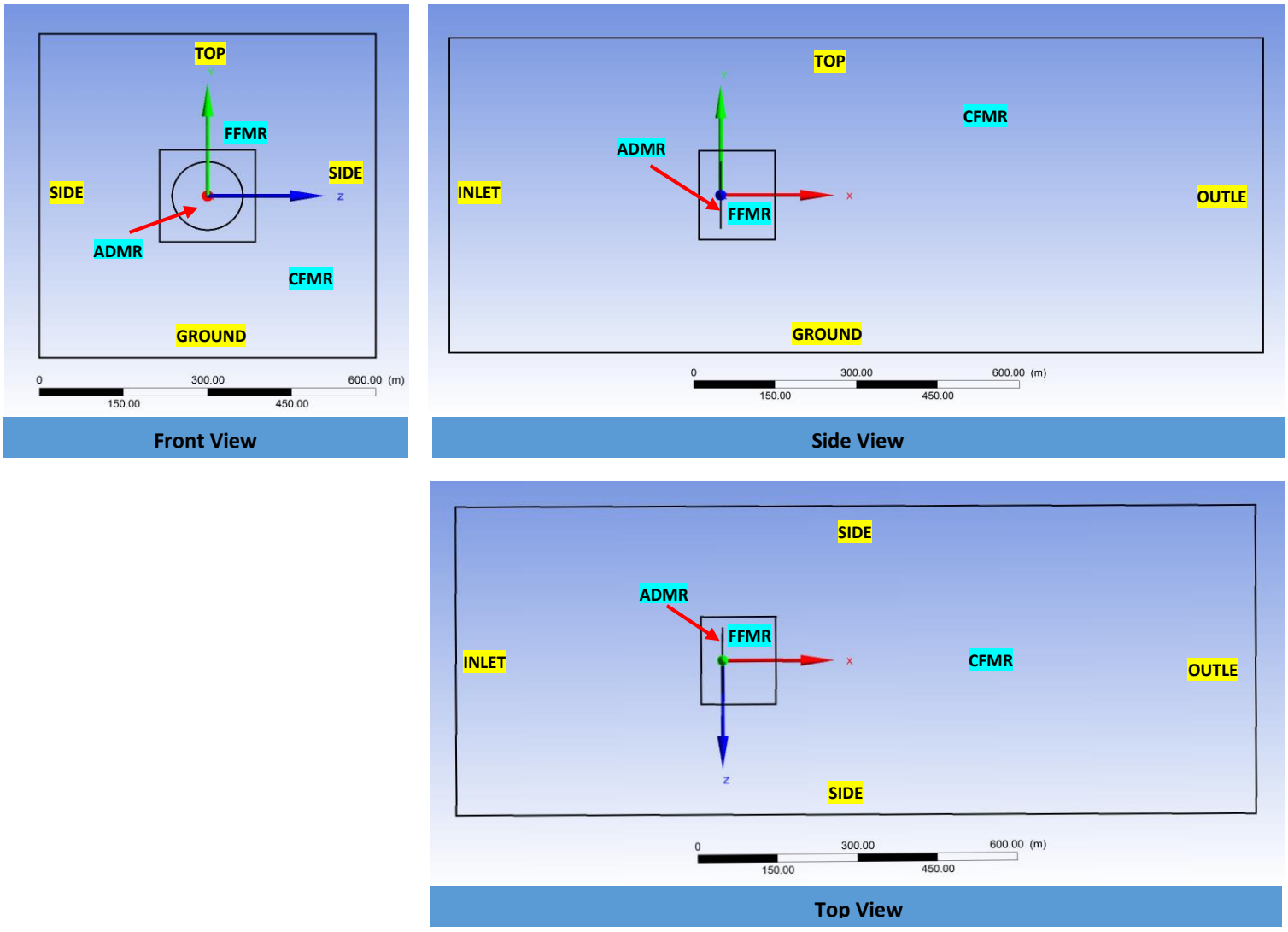

Figure 12: Front, side and top views of flow field setup showing the meshes and the boundaries

6.2.1 Inlet:

The boundary type for this boundary is set to “Inlet” in the ANSYS-CFX Pre. The direction constraint of “Inlet” boundary type requires that the flow direction is parallel to the boundary surface normal. Uniform velocity is applied to this boundary with no turbulence.

6.2.2 Outlet:

This boundary has a boundary type of “outlet” defined in ANSYS-CFX. At this boundary, a relative static pressure of 0 Pa is applied.

6.2.3 Top:

This boundary is the top surface of the fluid domain. It is defined by boundary type of “Opening” in ANSYS-CFX Pre. An opening boundary condition allows the fluid to cross the boundary surface in either direction. For example, all of the fluid might flow into the domain at the opening, or all of the fluid might flow out of the domain, or a mixture of the two might occur. At this boundary, a relative static pressure of 0 Pa is applied.

6.2.4 Ground:

This boundary defines the bottom of the fluid domain. It is defined by boundary type of “Wall” in ANSYS-CFX Pre. The fluid cannot cross this boundary. Free slip condition is used for this wall. In this case, the velocity component parallel to the wall has a finite value (which is computed), but the velocity normal to the wall, and the wall shear stress, are both set to zero.

6.2.5 Sides:

These boundaries define the two sides of the fluid domain. They are defined by boundary type of “SYMMETRY” in ANSYS-CFX Pre. The symmetry boundary type imposes constraints that ‘mirror’ the flow on either side of it. For example, the normal velocity component at the symmetry plane boundary is set to zero and the scalar variable gradients normal to the boundary are also set to zero

6.3 Mesh structure of fluid domain

The six boundaries defined above confines 3 types of mesh regions. These are a fine field mesh region, a coarse field mesh region and the actuator disc mesh region. These 3 mesh regions are shown in the Figure 12.

6.3.1 Actuator disc mesh region (ADMR)

The actuator disc, replacing the fully resolved turbine geometry, is inserted in the flow field not as a solid body but as a mesh. This is because the solid body will prevent the flow to pass through it. On the other hand, the mesh will allow the flow to pass through it. But to impart the same effect on the fluid as that of a fully resolved turbine geometry, momentum source terms are applied in this region of the mesh. The radius of the actuator disc mesh complies exactly with the radius of the turbine, which is 63 m. The thickness of the actuator disc mesh is set to 0.1 m. Thickness less than 0.1 m causes problems in the convergence of the analysis.

Figure 13 shows the front view of the actuator disc mesh. It can be seen from this figure that the actuator disc mesh a has a finer resolution near the tip region as compared to the region between the hub and the tip. This is because some of the flow variables, like axial and tangential induced velocities and angle of attack, change steeply near the tip region and a finer mesh resolution at the tip region helps to a more accurate prediction of flow characteristics. For the mesh statistics of this region, we refer to Table 3.

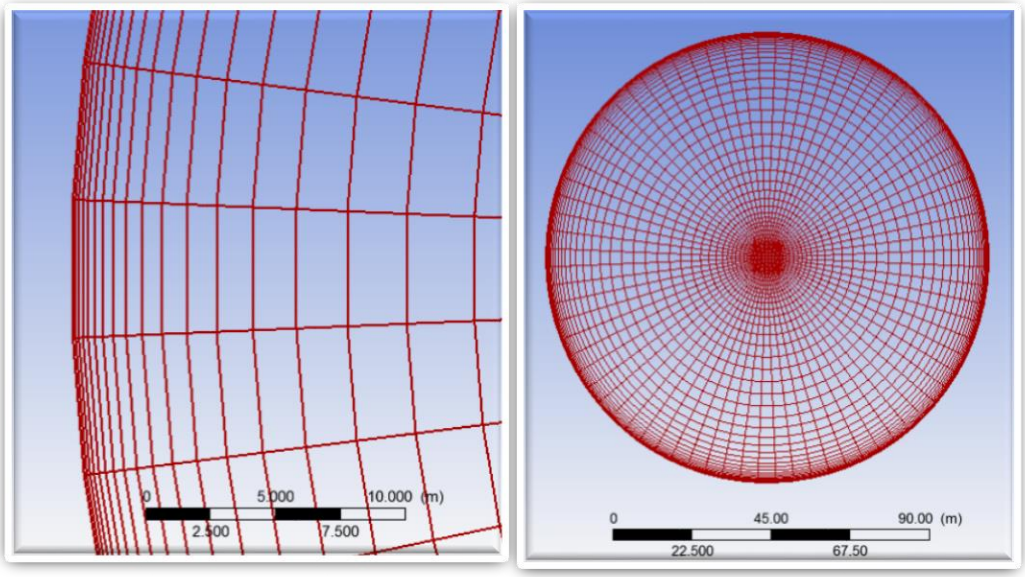

Figure 13: Front view of actuator disc mesh. Right diagram shows full mesh. Left diagram shows zoomed in tip region

6.3.2 Fine field mesh region (FFMR)

As seen in Figures 11 and 12, there is a fine field mesh region around the actuator disc mesh. This region of the fluid domain has a finer mesh resolution as compared to rest of the fluid domain (coarse field mesh region). The flow characteristics change rapidly in the vicinity, both upstream and downstream, of the actuator disc and to accurately capture these rapidly changing flow characteristics, a finer mesh resolution is used. For the mesh statistics of this region, we refer to Table 3.

Mesh regions	Actuator disc	Fine field mesh	Coarse field mesh
Number of nodes	26789	239465	599432
Hexahedra	23872	226152	573860
Volume (m^3)	1258.72	4.0734e+6	5.35954e+8

Table 3 : Mesh Statistics

6.3.3 Coarse field mesh region (CFMR)

The fluid domain around the actuator disc mesh region and the fine field mesh region is the coarse field mesh region. It has a coarser mesh resolution as compared to the mesh resolution of fine field mesh region. A coarser mesh resolution is used in this region to make the simulations computationally more efficient. Flow characteristics change rapidly only around the actuator disc and hence a finer mesh resolution is used in that region. In the rest of the fluid domain, the change in flow characteristics is relatively gradual and the

use of coarser resolution yields both accurate results as well as efficient computation. For the mesh statistics of this region, we refer to Table 3.

6.4 Mesh dependence check

For a mesh dependence check, three meshes are used, coarse mesh, medium mesh and fine mesh. The mesh statistics are given in Table 4. Simulations are performed with these three meshes using CFD-BEMT model for TSR = 4 and TSR = 6. The power and thrust coefficients are compared for different meshes to check mesh sensitivity. The results are shown in tabular form (Table 5) as well as graphical form (Figure 14).

Clearly, the performance remains fairly constant for the different meshes. The variation in performance is more pronounced at higher TSR. In this thesis, a medium mesh resolution is used.

	Coarse	Medium	Fine
ADMR	14792	23872	41864
FFMR	141956	226152	549286
CFMR	235420	573860	1990440
Total	392168	823884	2581590

Table 4: Number of Hexahedra for different mesh regions

	TSR = 4		TSR = 6	
Mesh	CP	CT	CP	CT
Coarse	0.224493	0.378085	0.459224	0.639462
Medium	0.224858	0.377768	0.461813	0.643123
Fine	0.224707	0.37795	0.461459	0.642109

Table 5: Performance comparison for different mesh types

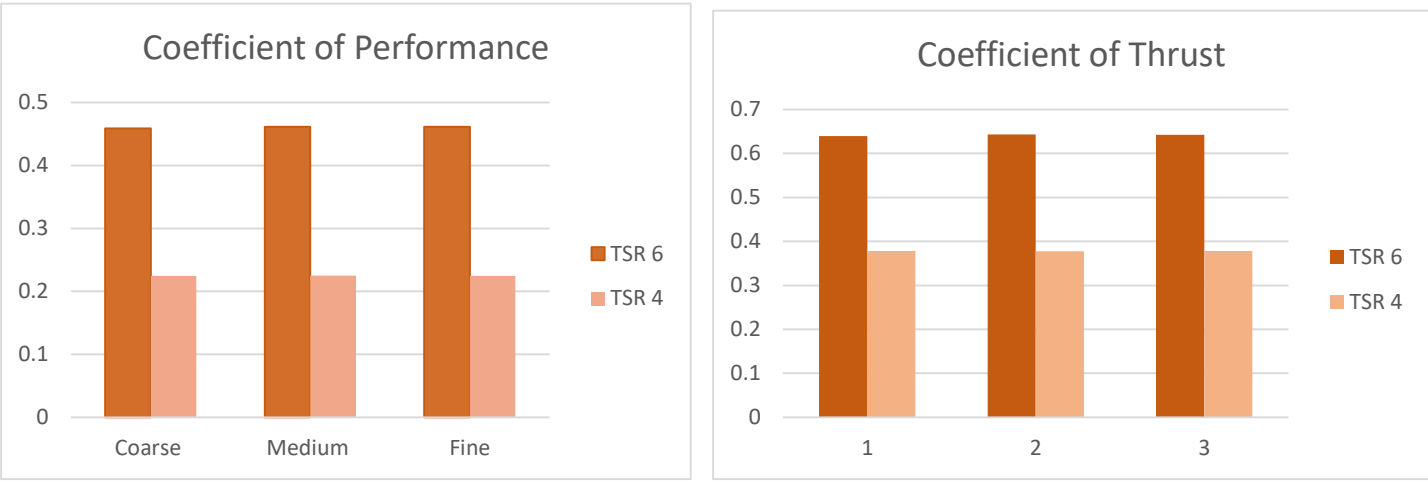

Figure 14 : Performance comparison for different mesh types

6.5 The FORTRAN Code to calculate momentum source terms.

The BEMT and the LLT are applied using FORTRAN code coupled to ANSYS CFX. The flow chart showing the working of the code is given in Figure 15. There are three important subroutines in the FORTRAN code which are used for the implementation of the model. These three subroutines are named Value_readin, Source_Term and Lifting_Line subroutines. A brief description of these subroutines are also given below.

6.5.1 Value_Readin Subroutine

This subroutine is called only once at the start of simulation. This subroutine reads the input files. Input data include TSR, hub radius, tip radius, number of blades, number of lifting line elements, airfoil geometry distribution (distribution of chord, pitch and airfoil used along the radius) and airfoil data (α, C_L and C_D data) of the 8 airfoils used in the simulation. After reading the data, this subroutine stores the data in the memory management system (MMS) of ANSYS-CFX. The data is later retrieved from the MMS in the Source_Term subroutine and is used in further calculations.

6.5.2 Lifting_Line Subroutine

This subroutine is called by Source_Term_subroutine only if the control volume lies in the BEMT+LLT region. This subroutine applies Lifting line theory and gives as an output, a matrix of dimensions (lifting line elements X 3). Three columns of the matrix are non-dimensional radial locations of lifting line elements, axial Induction factors and tangential induction factors. This matrix is used by the Source_Term subroutine to calculate momentum source terms and additional momentum source terms in BEMT+LLT region. Lifting Line theory is applied using a standalone FORTRAN code already developed at IST, Lisbon. The structure of the code was adapted to make it compatible with ANSYS-CFX.

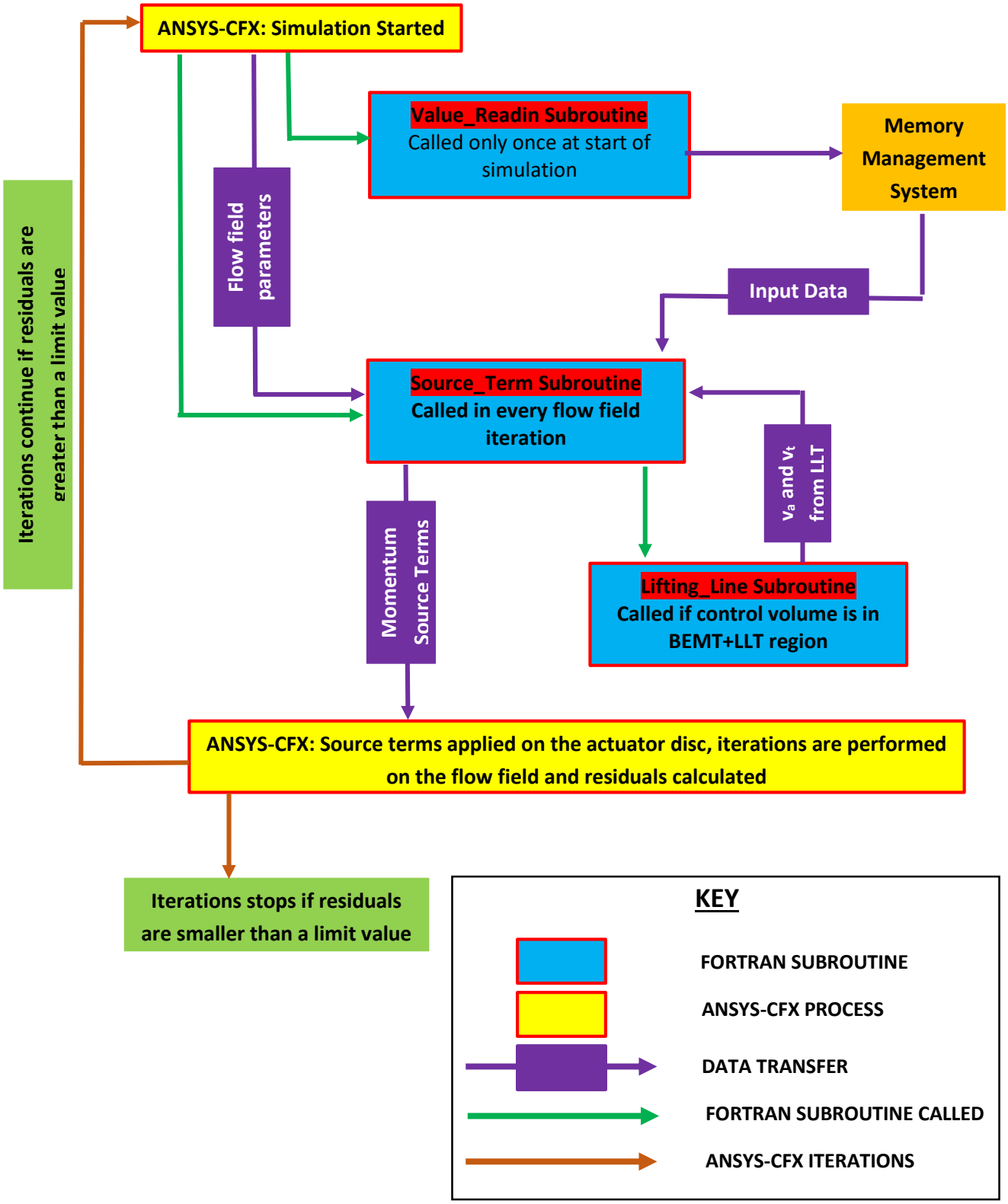

Figure 15: Flow chart for implementation of momentum source terms

6.5.3 Source_Term Subroutine

This subroutine calculates the momentum source terms for every control volume of actuator disc. It calculates the momentum source terms using the data stored in MMS by Value_readin subroutine, the current flow field data provided by ANSYS-CFX and the data provided by Lifting_Line subroutine.

CHAPTER 7: SIMULATION RESULTS AND DISCUSSION

7.1. Overview of the chapter

In this chapter, results of simulations conducted with five different CFD models are presented and discussions are made for single turbine and two turbines in a row. The five models are:

1. *CFD-BEMT* model which is a hybrid of CFD and BEMT.
2. *CFD-BEMT TL* model which is a hybrid of CFD and BEMT with the Prandtl tip loss factor.
3. *CFD BEMT+LLT M1* model which is an enhanced actuator disc model with the additional momentum source terms derived from Method 1.
4. *CFD BEMT+LLT M2* model which is an enhanced actuator disc model with the additional momentum source terms derived from Method 2.
5. *CFD BEMT+LLT M3* model which is an enhanced actuator disc model with the additional momentum source terms derived from Method 3.

In the first part of this chapter, the results obtained from simulations for the single turbine case will be presented for all five CFD models. Results for performance are compared with the reference result obtained from FAST V8 code. Results for the local flow field parameters at the turbine are compared with the results obtained from LLT IST code.

In the second part of this chapter, performance results for the downstream wind turbine obtained from simulations of two turbines in a row are presented. The idea is to find out how the performance of a downstream wind turbine is effected by the presence of an upstream wind turbine. The results obtained from the five different CFD models are only compared with each other because reference results are not available, either experimental or from any commercial software tool, for downstream wind turbine.

7.2 Results and discussion for one turbine case

The following results and discussions are included in this section.

1. Performance: C_P and C_T.
2. Local Flow field parameters; axial and tangential induction factors, α and C_D, along the span of the turbine blade.
3. Axial velocity field.
4. Tangential velocity field.
5. Turbulence Kinetic Energy.

7.2.1 Performance

7.2.1.1 Power Coefficient

Figure 16 shows the variation in C_P with TSR. The reference results from FAST V8 are also presented in this figure. FAST- BEMT and CFD-BEMT models have higher C_P throughout the range of TSR presented except for TSR = 9 where the C_P predicted from CFD-BEMT+LLT M3 is higher than C_P predicted from Fast BEMT.

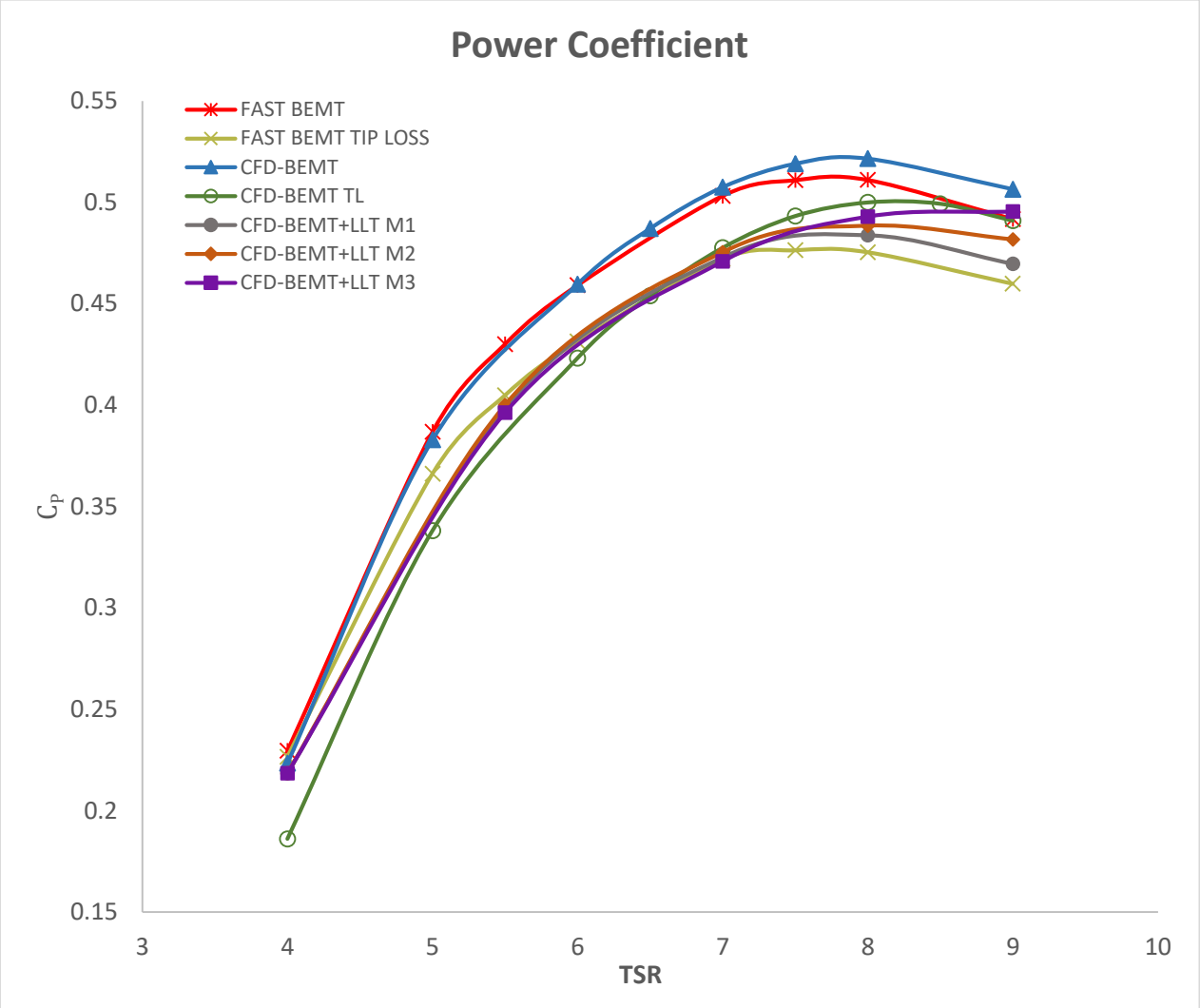

Figure 16: Variation of power coefficient with TSR

C_P predicted from Fast BEMT and CFD-BEMT are in good correlation from TSR = 4 to TSR = 7. Above TSR = 7, CFD-BEMT over predicts C_P compared to FAST BEMT and the difference increases with the increase in TSR.

CFD-BEMT TL under predicts C_P as compared to C_P from FAST BEMT with tip loss from TSR = 4 to TSR = 6.5. At TSR = 6.5 C_P predicted from CFD-BEMT TL and FAST BEMT with tip loss almost coincides. Above TSR = 6.5, CFD-BEMT TL over predicts C_P compared to FAST BEMT with tip loss and the over prediction further increases with increase in TSR.

C_P predicted from CFD-BEMT+LLT M1, CFD-BEMT+LLT M2 and CFD-BEMT+LLT models show good correlation from TSR = 4 to TSR = 7. Above TST = 7, C_P values predicted from these methods start to deviate from each other with the C_P from CFD-BEMT+LLT M3 model being the highest and from CFD-BEMT+LLT M1 being the lowest. These three enhanced actuator disc models under predict C_P compared to FAST BEMT with tip loss from TSR = 4 to TSR = 5.5. From TSR = 5.5 to TSR = 7, C_P predicted from enhanced actuator disc models and from FAST BEMT with tip loss shows good correlation. Above TSR = 7, the enhanced actuator disc models over predict C_P as compared FAST BEMT with tip loss.

For all models except CFD-BEMT+LLT M3, maximum C_P lies either at TSR = 7.5 or at TSR = 8. But for CFD-BEMT+LLT M3 model, maximum C_P lies at TSR = 9 and it may further increase above TSR =9.

7.2.1.2 Thrust coefficient

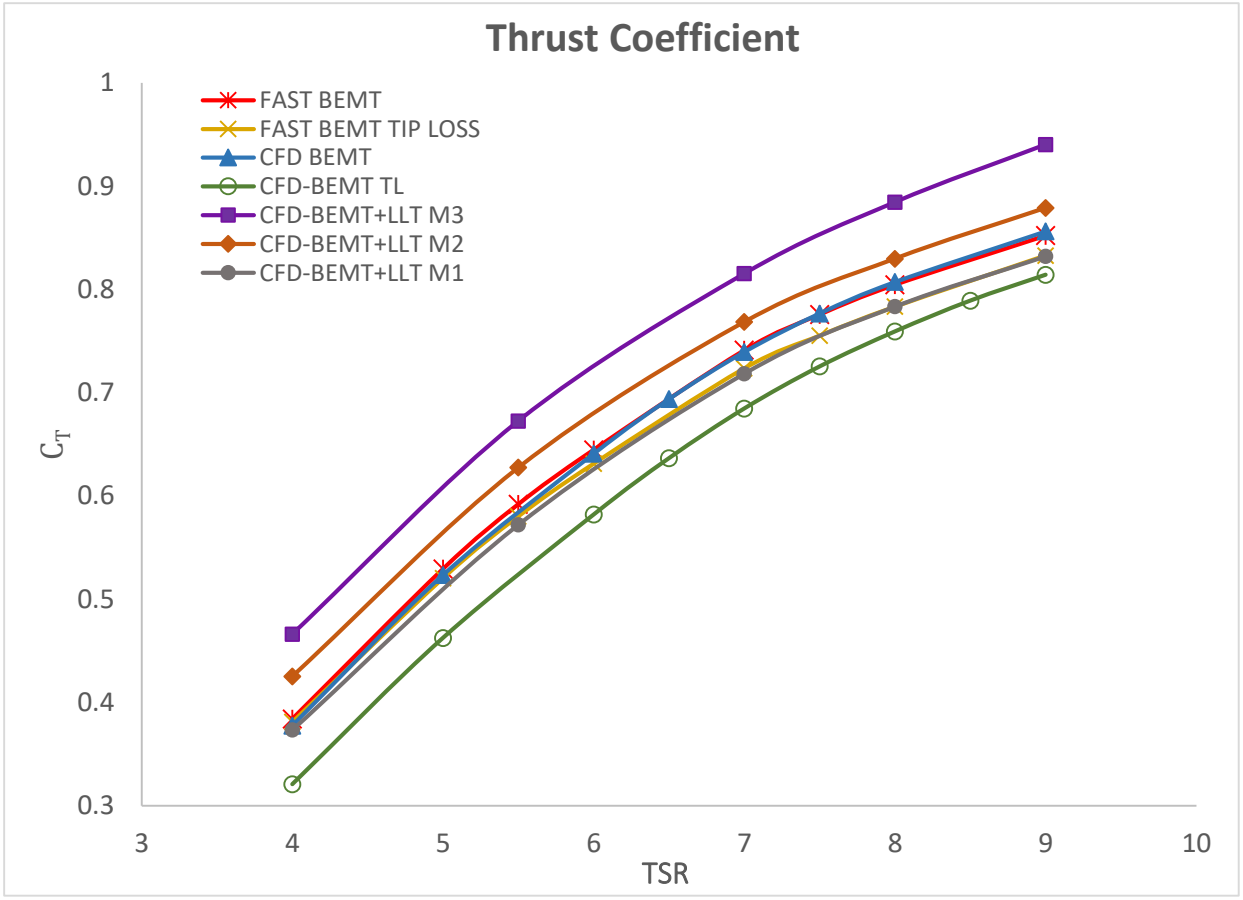

Figure 17: Variation of thrust coefficient with TSR

Figure 17 shows variation of C_T with TSR. Reference results from FAST V8 are also presented in this figure. It is observed that for all five CFD models and for reference results, C_T increases with increase in TSR. It is very clear from this figure that at a particular TSR, the CFD model with higher momentum source terms will have a higher C_T and vice versa. CFD-BEMT TL has reduced axial force throughout the blade span due to the tip loss effect as compared to other methods, hence its axial momentum source terms and its C_T is lowest for all TSRs presented here. CFD-BEMT+LLT M3 model has the highest axial source terms in the BEMT+LLT region, therefore it has highest predicted values of C_T as compared to all other methods at all TSRs presented. Similar is the case with CFD-BEMT+LLT M2 model. The momentum source terms for CFD-BEMT+LLT M2 model in tip region are higher than those for CFD-BEMT, CFD-BEMT TL and CFD-BEMT+LLT M1 models, so C_T predicted from CFD-BEMT+LLT M2 model is also higher than CFD-BEMT, CFD-BEMT TL and CFD-BEMT+LLT M1 models.

Further it is observed that C_T predicted from FAST BEMT and CFD-BEMT are in very good correlation throughout the range of TSR presented. However, C_T predicted from FAST BEMT with tip loss effect is not in good correlation with C_T predicted from CFD-BEMT TL. C_T calculated from CFD-BEMT TL is lower as compared to C_T calculated from FAST BEMT with tip loss effect throughout the range of TSR presented. Rather C_T predicted from CFD-BEMT+LLT M1 and FAST BEMT with tip loss are in strong correlation throughout the range of TSR.

7.2.2 Local Flow field parameters

7.2.2.1 Axial induction factor

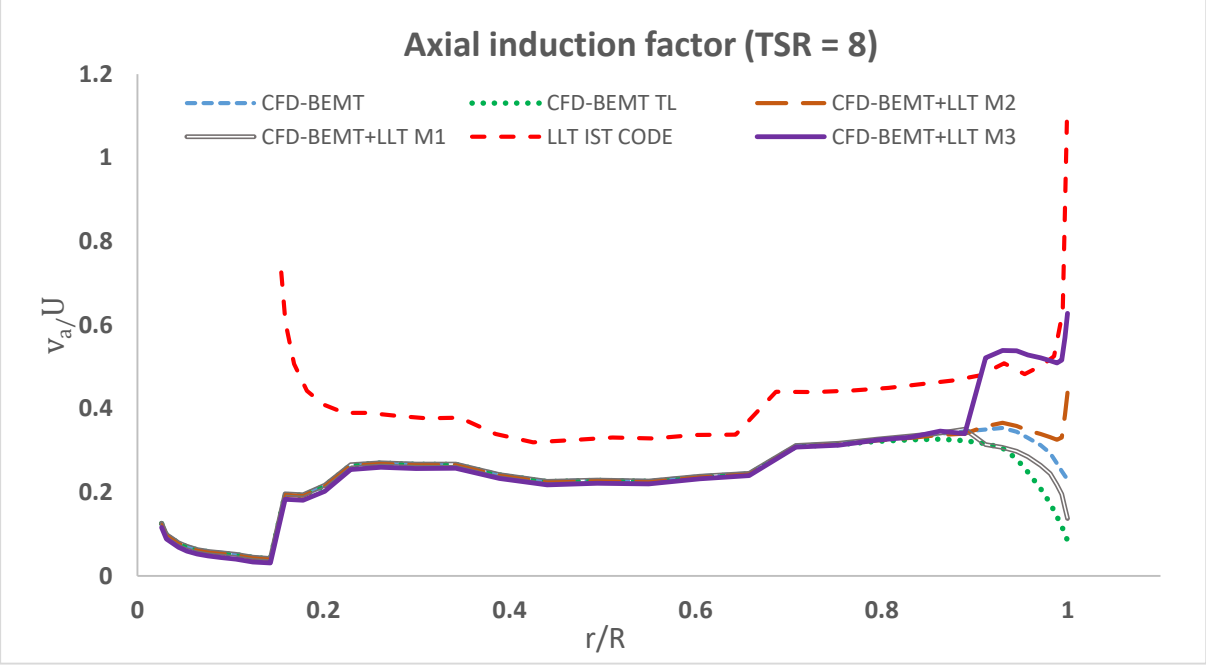

Figure 18: Variation of axial induction factor with dimensionless radial distance at TSR = 8

Figure 18 represents the variation of the axial induction factor with dimensionless radial distance at TSR = 8. Results from the LLT IST code are used for comparison. As expected, all CFD models predict lower axial induction factors throughout the span of turbine blade in comparison with the Lifting line. In the tip region, CFD-BEMT TL has the lowest axial induction factors due to reduced forces resulting from the tip loss effect. The axial induction factor in the tip region approaches the Lifting line for CFD-BEMT+LLT M2 and CFD-BEMT+LLT M3 models. CFD-BEMT+LLT M3 model has the highest additional momentum source terms and hence has the highest axial induction factors in the tip region. Even axial induction factors in BEMT+LLT region for this model are higher than those from LLT IST except at the very tip end. Still at the very tip end, CFD-BEMT+LLT M3 model is not capable to predict high axial induction factors as are predicted with LLT IST code. One reason for this is that, ANSYS-CFX is based on control volume approach and hence instead of calculating axial induction factor at the very tip end, it calculates an average of the axial induction factors in the last cell towards the tip end. The value of the axial induction factor at the very tip end will be higher than the average value calculated for the last control volume. For CFD-BEMT+LLT M1, flow field prediction in the tip region is rather poor and axial induction factors are smaller even as compared to those obtained from BEMT-CFD model. This is because additional momentum source terms for CFD-BEMT+LLT M1 method are very small and hence do not have a strong impact. Near the blade root, all CFD models behave opposite to LLT IST code. LLT IST code predicts high axial induction factors at the root, to achieve zero lift condition like the tip end, while the CFD models predict low axial induction factors near the root.

7.2.2.2 Tangential Induction Factor

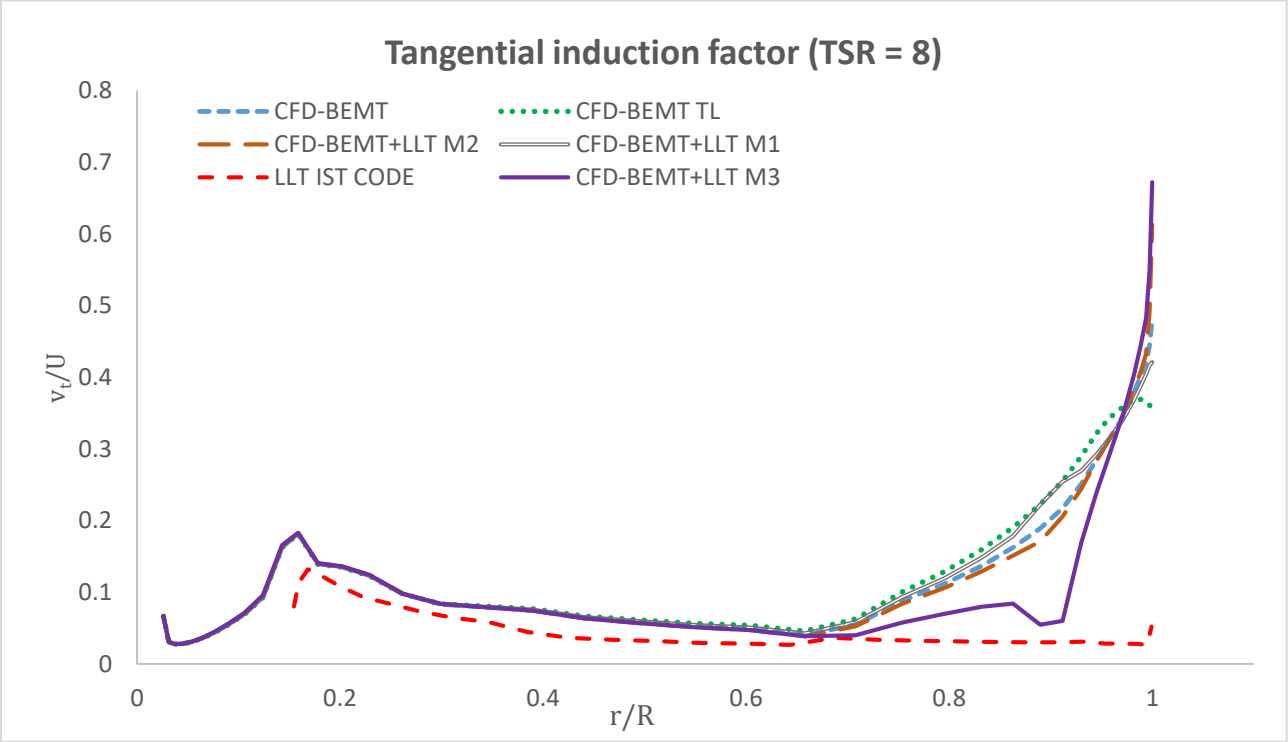

Figure 19: Variation of tangential induction factor with dimensionless radial distance at TSR = 8

Figure 19 shows the variation of tangential induction factor with dimensionless radial distance at TSR = 8. Here it is important to mention that the tangential induction factors are obtained by dividing tangential velocity with incoming freestream air velocity (not by dividing tangential velocity by 2Ω, which is the usual case). From r/R = 0.2 to r/R = 0.7, all CFD models slightly over predict tangential induction factor as compared to LLT IST code. However above r/R = 0.7, particularly at the tip region, CFD models over predict tangential induction factors compared to LLT IST code to large extents. For enhanced actuator disc models, the effect of additional momentum source terms is to reduce the tangential induced velocities near the tip region and match them to those obtained from LLT IST code. That is why there is a dip in the values of tangential induction factors predicted from CFD-BEMT+ LLT M3 model near r/R = 0.9. After the dip the tangential induction factors rise sharply and at the tip it is even larger than the tangential induction factors predicted from CFD-BEMT and CFD-BEMT TL models. The reason for this rising trend of tangential induction factor near the tip is still unclear. CFD-BEMT+LLT M2 model also follows similar trend as CFD-BEMT+LLT M3 model but the dip and rise trend in induction factor near the tip is very small as compared to the trend from CFD-BEMT+LLT M3 model.

7.2.2.3 Angle of Attack

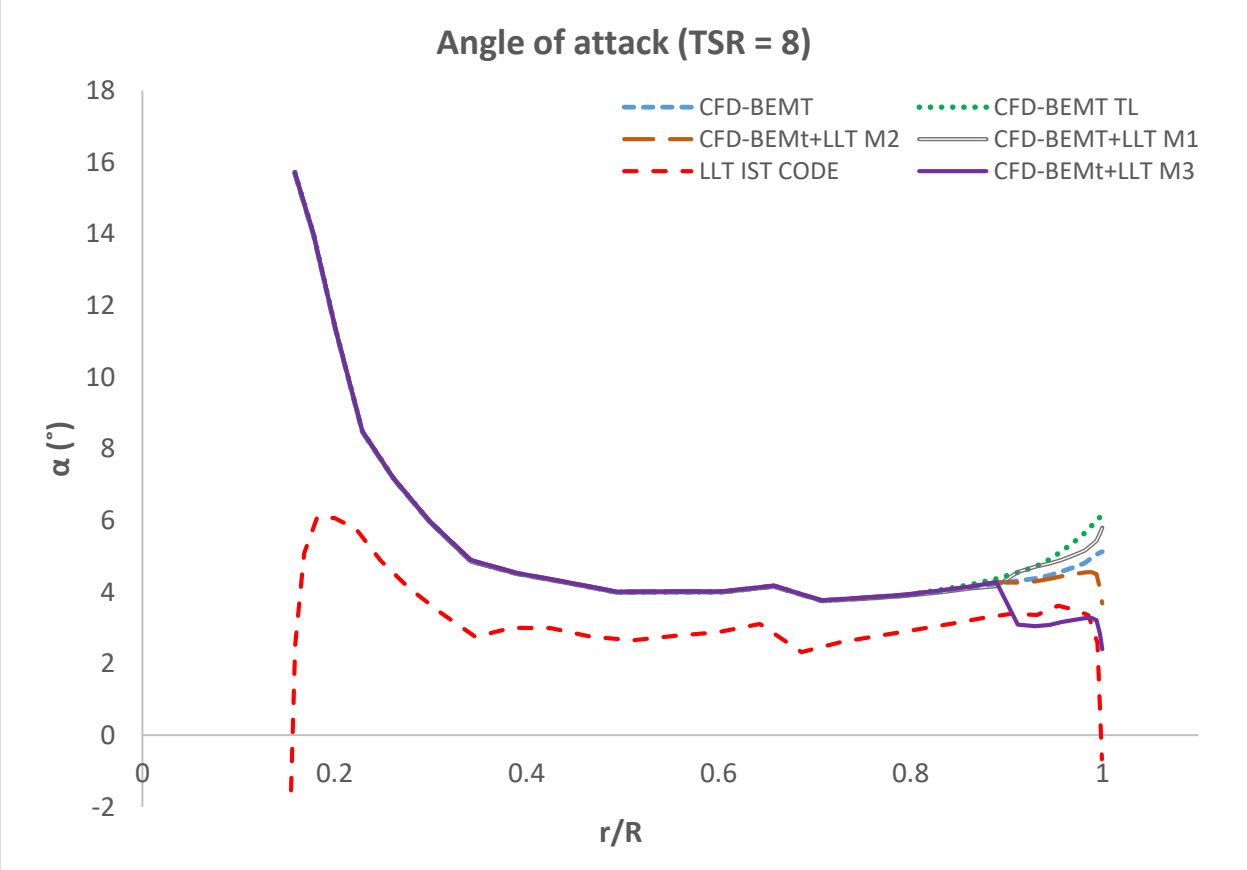

Figure 20: Variation of angle of attack with dimensionless radial distance at TSR = 8

Figure 20 represents the variation of angle of attack, α, with dimensionless radial distance at TSR = 8. Results from LLT IST code are used for comparison. According to LLT, the angle of attack at the tip region should reduce to a value that generates zero lift condition. That is why the angle of attack from LLT IST codes shows a sharp decrease at the tip region. Except CFD-BEMT+LLT M3 model, all CFD models predict higher α throughout the length of turbine blade as compared to LLT IST code. In most of the BEMT+LLT region, CFD-BEMT+LLT M3 slightly under predicts the angle of attack compared to LLT IST code.

Although α for zero lift condition (as predicted by LLT IST code) is not achieved with any CFD model, clearly the prediction of α in the tip region is improved with CFD-BEMT+LLT M2 and CFD-BEMT+LLT M3 models as compared to CFD-BEMT, CFD-BEMT TL and CFD-BEMT+LLT M1 models. CFD-BEMT+LLT M1 model has very small additional momentum source terms in the tip region and hence prediction of α with this method is poor even as compared to CFD-BEMT method. α prediction from CFD-BEMT TL model is highest in the tip region because the tip loss reduces the blade forces which in turn results in poor prediction of induced velocities and hence α.

Overall, in the tip region, predictions of α from CFD-BEMT+LLT M3 model follow the results from LLT IST code to highest degree and predictions from CFD-BEMT TL model follow these results to lowest degree.

Further, again it can be observed that the predictions from CFD models and LLT follow opposite trend in the root region because in the LLT, the condition of zero lift at the root must be met.

7.2.2.4 Drag coefficient

Figure 21 represents variation of C_D with dimensionless radial distance at TSR = 8. Results from LLT IST code are used for comparison. Predictions of C_D form all CFD models show good correlation with C_D obtained from LLT IST code for most part of the blade length from r/R = 0.4 to r/R = 0.9.

For r/R smaller than 0.3, all CFD models considerably over predict C_D compared to LLT IST code. This is because at the hub region, angle of attack prediction from CFD models are high as compared to angle of attack predictions from LLT IST code and higher angles of attack leads to higher C_D for the airfoils used in that region (DU21_A17 and DU25_A17).

At the tip region C_D predicted from CFD BEMT, CFD-BEMT+LLT M3 and CFD-BEMT+LLT M2 models show very good correlation with C_D predicted from LLT IST code. CFD-BEMT TL and CFD-BEMT+LLT M1 slightly over predicts C_D compared to LLT IST code with the predictions from CFD-BEMT TL model being the highest. These over predictions of C_D from CFD-BEMT TL and CFD-BEMT+LLT M1 models are due to higher angles of attack predicted from these models as compared to angles of attack predicted from other CFD models in the tip region

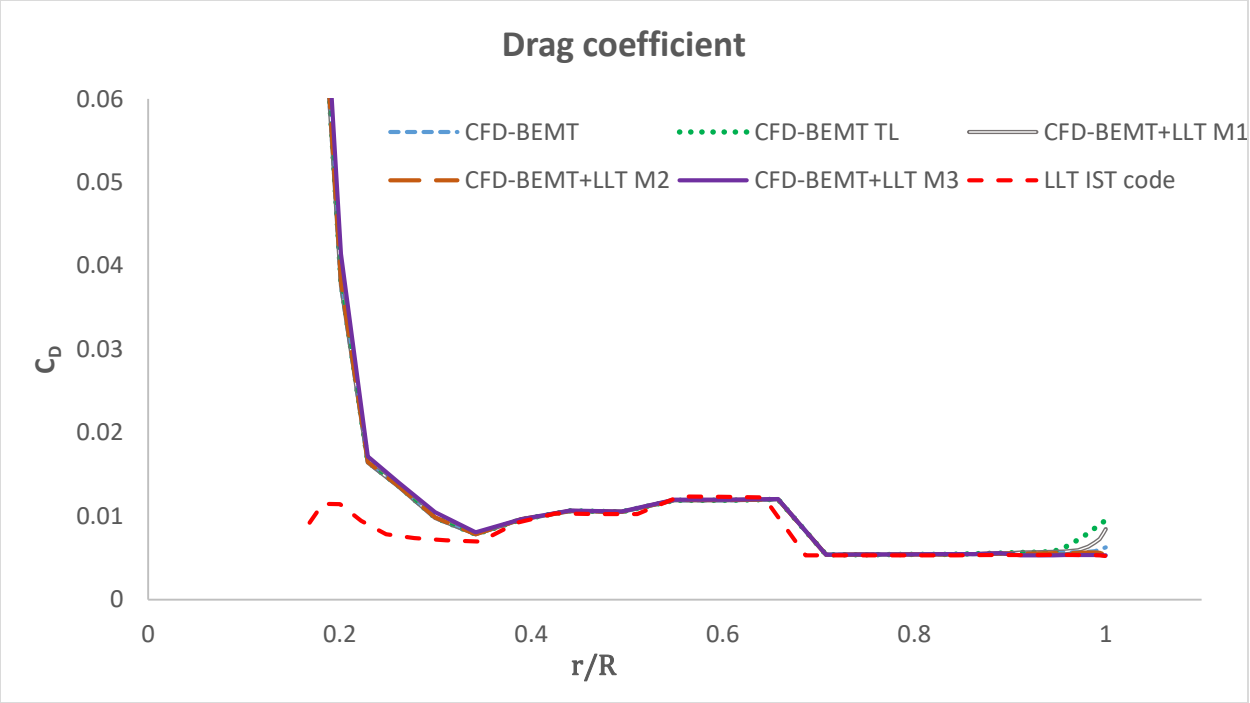

Figure 21: Variation of the drag coefficient with dimensionless radial distance at TSR = 8

7.2.3 Axial velocity field

7.2.3.1 Average axial velocity upstream and downstream of the turbine

Figure 22 shows the variation of average axial velocity plotted against axial distance (x-coordinate) upstream and downstream of the turbine. The graph shows two sets of curves. One set of five curves (light colors) is for TSR = 8 and the other set of five curves (dark colors) is for TSR = 4. First of all, it can be clearly observed from the graph that, the higher the TSR, the greater the reduction in velocity from the upstream to the downstream side. This is because for higher TSRs, axial (thrust) forces are higher, axial reactive forces are higher and hence a larger reduction in axial velocity takes place.

Further, it can also be noted that generally, the higher the axial momentum source terms from a CFD method, the larger will be the reduction in velocity from the upstream side to downstream side. For TSR = 4, CFD-BEMT+LLT M3 has the highest axial momentum source terms in the tip region, therefore causing the largest reduction in velocity in this region (refer to Figure 24) and hence the greatest reduction in average velocity among all five CFD methods for TSR = 4. CFD-BEMT TL has the lowest axial momentum source terms throughout the length of blade due to tip loss effect, hence the reduction in velocity is the lowest. Similar is the case with the remaining three methods. It can also be seen that this graph also complies with the graph of C_T against TSR. The method with higher C_T has higher thrust, higher axial reactive force and hence greater reductions in axial velocity.

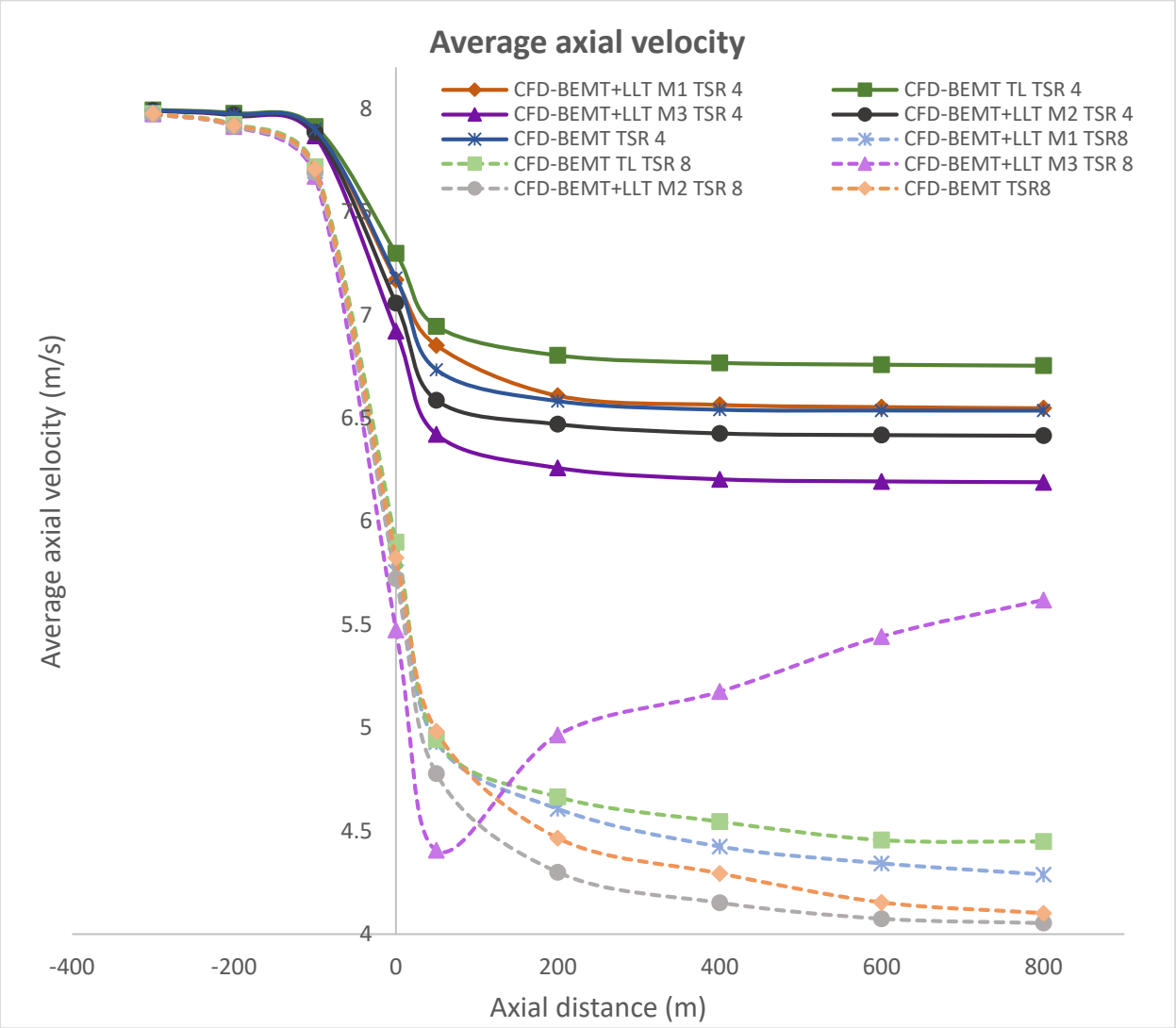

Figure 22: Variation of average axial velocity with axial distance for all CFD models at TSR 4 and TSR 8

For TSR = 8, generally the trend is same as that of TSR = 4. But there is one important behavior for CFD-BEMT+LLT M3 model that needs to be discussed. The decrease in average axial velocity is highest for this method till about 50 m downstream of the turbine, after that velocity starts to increase again. In figure 23, it can be seen in the plot of CFD-BEMT+LLT M3 model at TSR = 8 that negative velocity is achieved near the tip region at the downstream side very close to turbine. High reduction in velocity generates high shear between the wake boundary and undisturbed free stream air. This leads to turbulence generation which causes mixing of the wake with undisturbed free stream air and hence increases the velocity in the wake region. Turbulence generation can also be verified from turbulence plots in figure 28. The plot of CFD-BEMT+LLT M3 at TSR = 8 clearly shows high turbulence.

7.2.3.2 Axial Velocity field displayed on a longitudinal plane (xy-plane) passing through turbine center

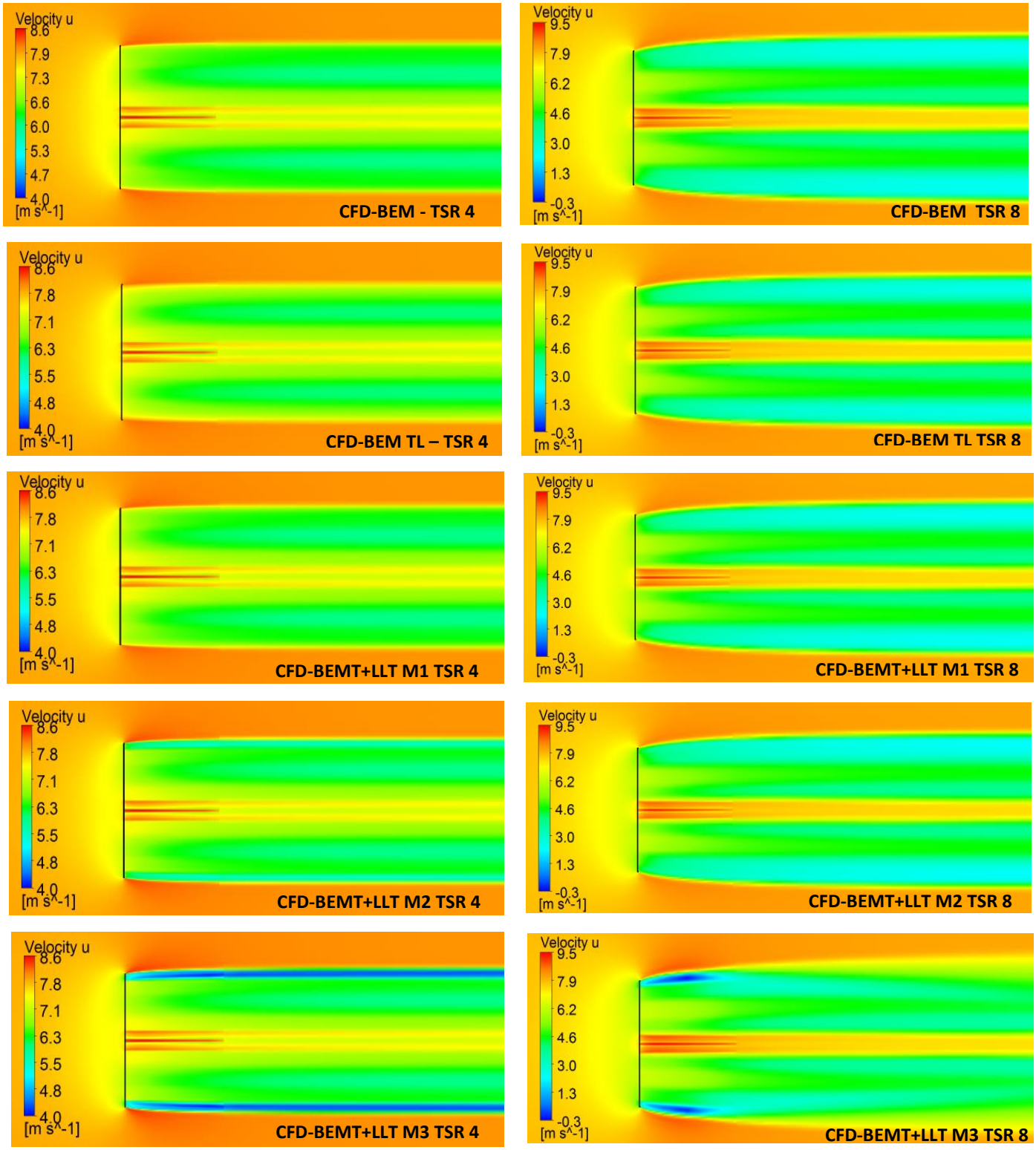

Figure 23: Axial velocity field shown on xy-plane for all CFD models at TSR 4 and TSR 8

Figure 23 shows the axial velocity field plotted on *xy*-plane for all CFD methods at TSR = 4 and TSR = 8. The scales for TSR = 4 plots and TSR = 8 plots are different for clarity purpose and to cover full range of velocities involved. TSR = 4 plots clearly show that velocities downstream of the turbine for CFD-BEMT TL model are higher than those obtained from CFD-BEMT model. This is obvious because in CFD-BEMT TL model, axial forces on blades are reduced due to tip loss effect throughout the length of blade and hence axial source terms are also small. This difference is not observable for TSR = 8 because TSR = 8 plots have scale of wider range.

Further, since the additional momentum source terms are very small for CFD-BEMT+LLT M1, there is not much observable difference between the plots for CFD-BEMT model and CFD-BEMT+LLT M1 at TSR = 4. This observation also complies with Figures 17, 18 and 22 where the differences in C_T, axial induction factor and average axial velocity respectively for these two models are very small for TSR = 4. For CFD-BEMT+LLT M3 model, axial momentum source terms are of highest magnitude at the tip region (BEMT+LLT region), hence there is a dark blue region at the downstream side of tip region clearly indicating high reduction in axial velocity in this region. For the CFD-BEMT+LLT M2 model, the additional momentum source terms are of medium level among the three enhanced actuator disc models, hence there is light blue color at the downstream side of tip region which indicates that velocity is decreased in this region but not as much as that for CFD-BEMT+LLT M3 model.

Lastly, the plot for CFD-BEMT+LLT M3 model at TSR = 8 shows that axial velocity at the downstream side near the turbine at the tip region has achieved negative value of about -0.3 m/s. This negative value is achieved because the additional momentum source terms are very high leading to huge reduction of velocity. But the velocity does not remain negative further downstream at tip region and it increases because as already mentioned in previous section of results, turbulence is generated which causes the velocity to increase.

7.2.3.3 Axial velocity field downstream of turbine at 200m and 600m

Figure 24 represents the variation of axial velocity along the y coordinate at z = 0 at a distance of 200m downstream of the turbine. The graph shows two sets of curves. One set of curve (dark colors) is for TSR = 4 and the second set of curves (light colors) is for TSR = 8. Here in these graphs, it is again experienced that generally the greater the TSR, the lower will be the value of velocity. The set of curves for TSR = 4 generally shows higher velocity than the set of curve for TSR = 8. Also it can be observed that when additional source terms are applied in the tip region for CFD-BEMT+LLT M2 and CFD-BEMT+LLT M3 models, velocity is more reduced in the tip region as compared to rest of the blade region. Velocity is lowest in the tip region for CFD-BEMT+LLT M3 as it has the highest axial momentum source terms at the tip region. Furthermore, CFD-BEMT+LLT M1 does not show reduction in velocity in the tip region as compared to CFD-BEMT since the additional momentum source terms are very small for this method. CFD-BEMT TL, as expected, shows the highest velocities in the outer blade region as compared to rest of the CFD models

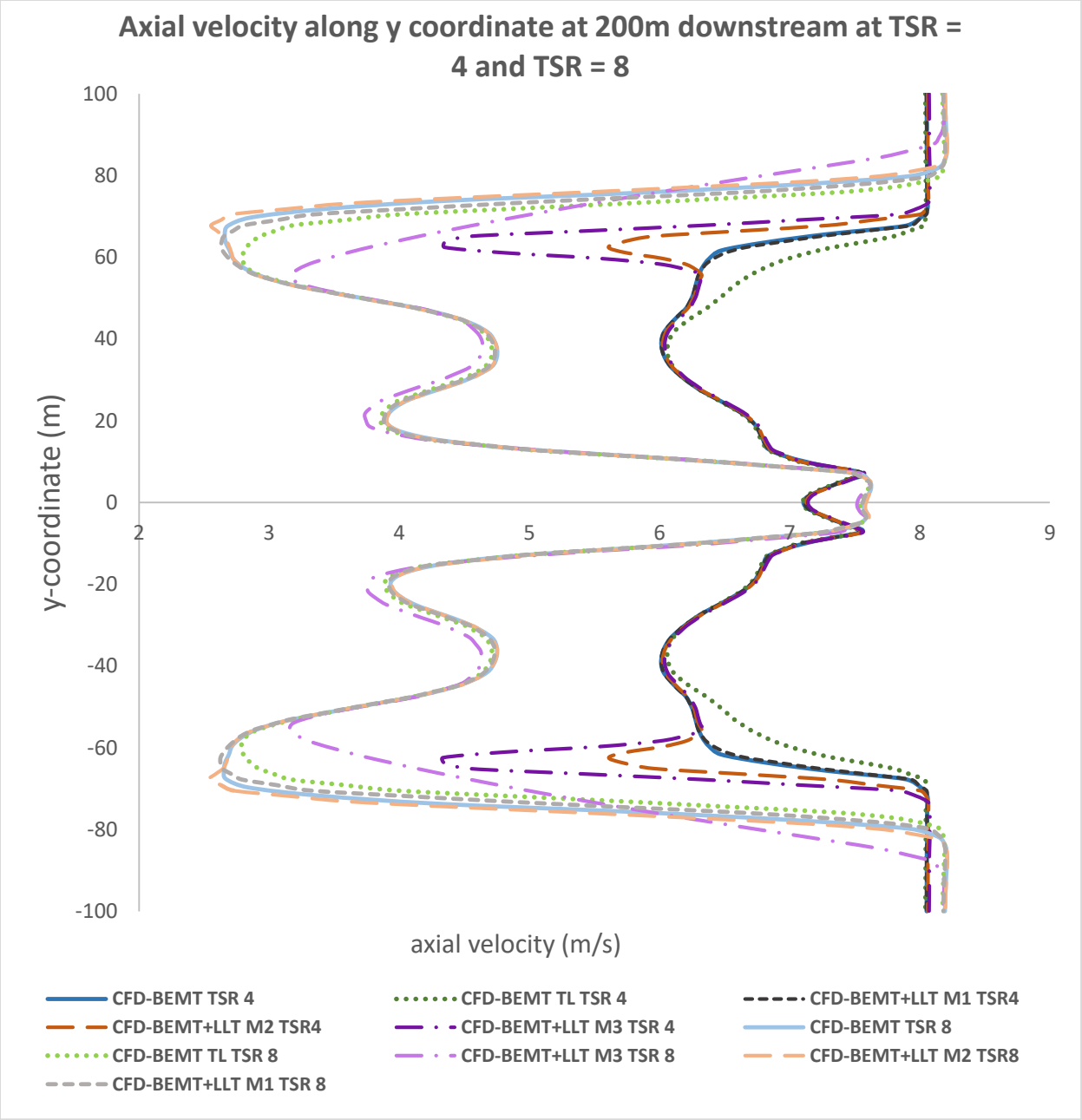

Figure 24: Variation of axial velocity along y coordinate at z = 0 at 200m downstream of turbine for TSR = 4 and TSR= 8

since the axial forces are reduced due to implementation of tip loss effect. For all CFD models, the axial velocities are highest in the center region because for Hub, Cylinder 1 and Cylinder 2 used in the center region of turbine, C_L is zero which leads to reduced axial reactive forces.

Furthermore, it is important to mention here that for CFD-BEMT+LLT M3 model at TSR = 8, the velocity in the tip region has already started to recover at 200 m downstream of the turbine due to turbulence. That is why in the tip region, axial velocities predicted from CFD-BEMT+LLT M3 model are higher than those predicted from rest of the CFD models. The same thing can be observed in Figure 25 which representing

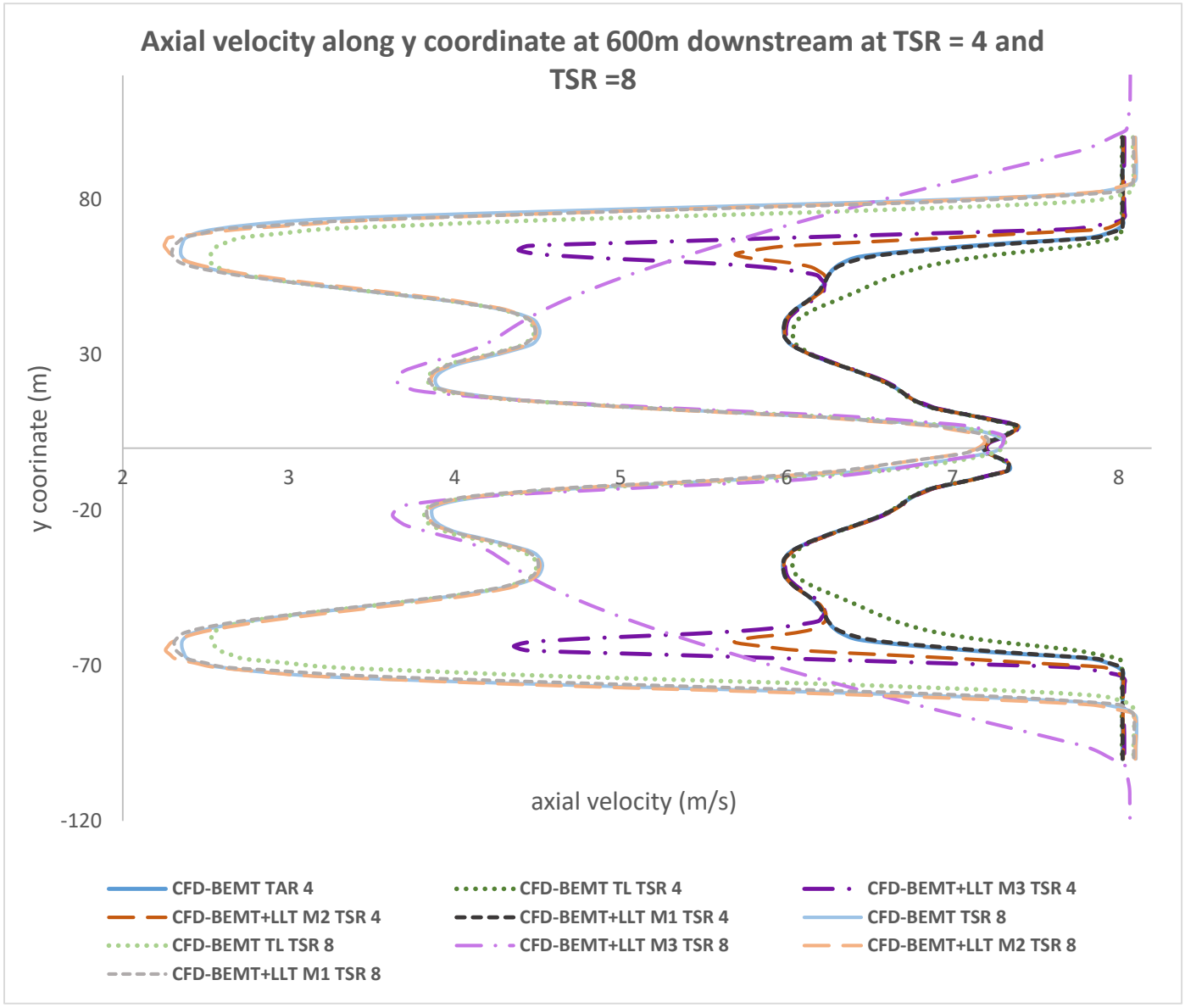

Figure 25: Variation of axial velocity along y coordinate at z=0 at 600m downstream of turbine for TSR = 4 and TSR = 8

the variation of axial velocity with the y coordinate at z = 0 at a distance of 600 m downstream of the turbine. The axial velocity profile for CFD-BEMT+LLT M3 model at TSR = 8 shows large recovery from velocity deficit generated due to extraction of energy by the turbine. Hence turbulence is very helpful in recovering the reduced velocities in the turbine wake.

Another observation can be made from Figures 24 and 25. The stream tube expands more at higher TSR. At TSR = 4, stream tube diameter is around 140 m in diameter at 200 m downstream of turbine while at TSR = 8, stream tube diameter is about 160 m at 200 m downstream of turbine. This is because at higher TSR, more energy is extracted from the wind and hence, the stream tube expands more in the process of recovering the negative pressure to atmospheric level at downstream side of turbine.

7.2.4 Tangential velocity downstream of the turbine

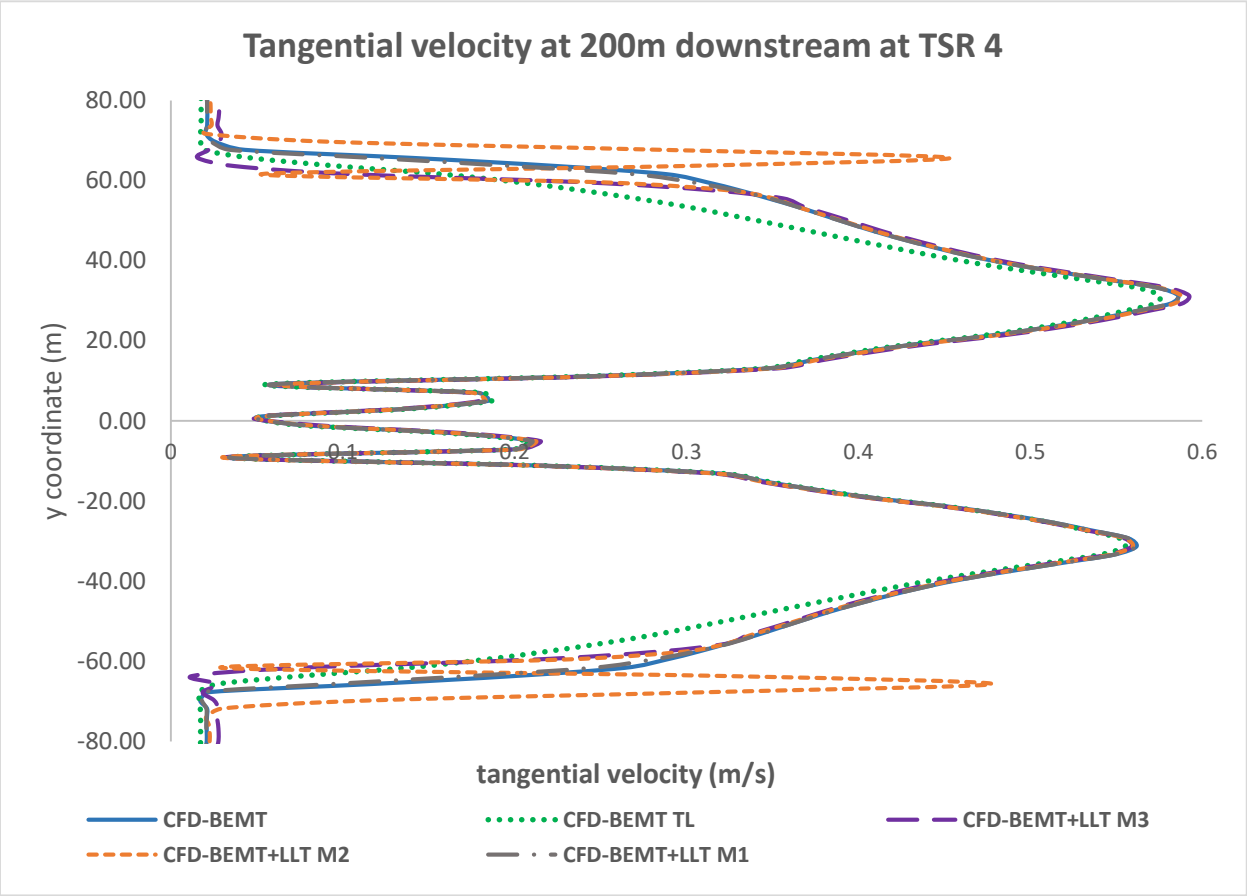

Figure 26: Variation of tangential velocity along y coordinate at z=0 at 200m downstream of turbine for TSR = 4

In Figures 26 and 27, the distribution of tangential induced velocities along y coordinate at 200 m downstream of the turbine for all CFD models are given for TSR = 4 and TSR = 8. Since the results are almost symmetric about the line y = 0 m, discussion will only be made for results along positive y-coordinate. For TSR = 4, the tangential induced velocities from all CFD methods almost coincide in the center region of wake from y = 0 to y = 40 m. In outer wake region beyond y = 40 m, CFD-BEMT TL clearly shows lower tangential induced velocities as compared to CFD-BEMT. This is evident as due to tip loss effect CFD-BEMT TL model has lower forces, particularly at the tip region of the turbine, as compared to CFD-BEMT model. From LLT IST code, tangential induced velocities are lower in magnitude as compared to those calculated from CFD-BEMT models (see Figure 19). Therefore, in CFD-BEMT+LLT M1, CFD-BEMT+LLT M2 and CFD-BEMT+LLT M3 models, the effect of additional momentum source term is to reduce the total momentum source terms as compared to CFD-BEMT model. Reduced total momentum source terms would generate lower tangential velocities. This effect can be clearly seen in the tip region of the wake for CFD-BEMT+LLT M3 model as additional momentum source terms are highest for this model. The CFD-BEMT+LLT M1 model has additional momentum source terms of very small magnitude, therefore tangential

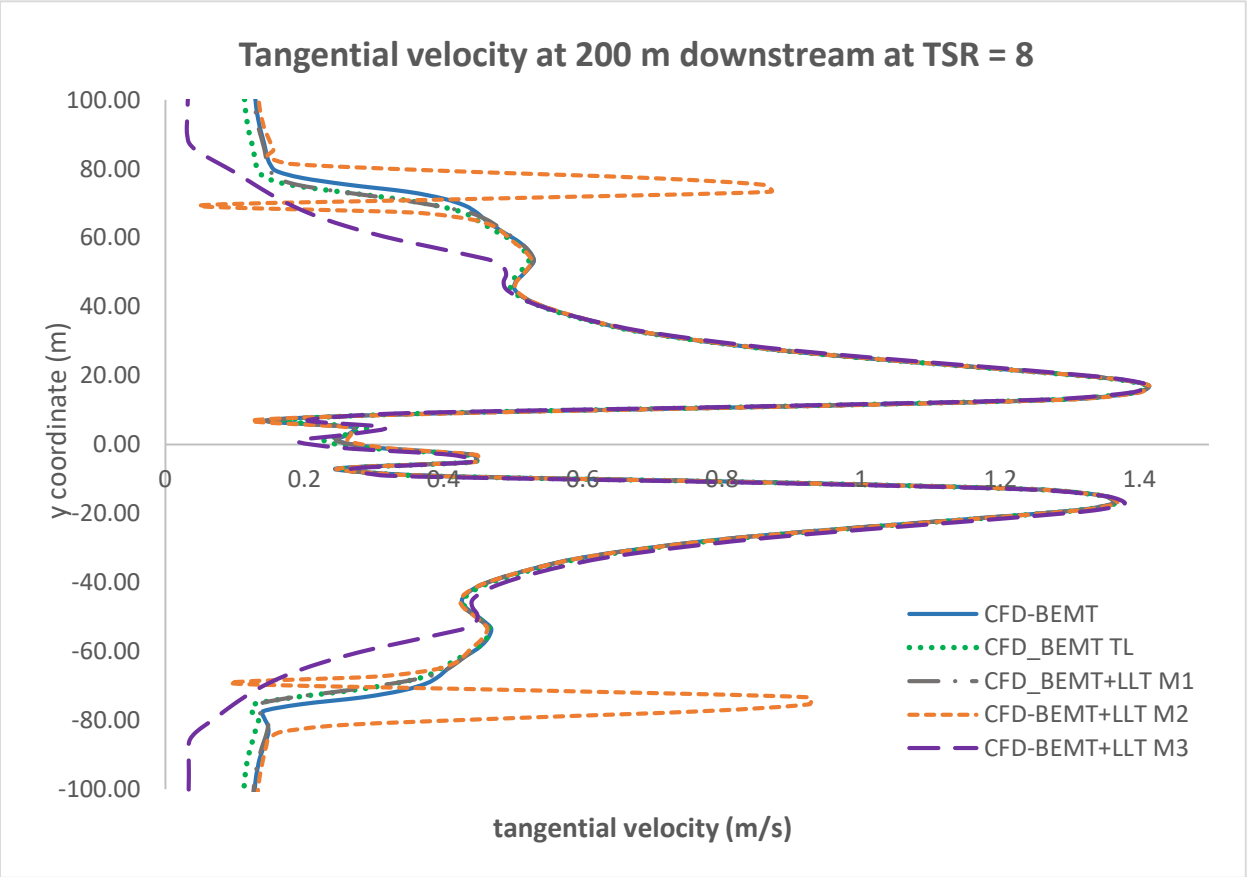

Figure 27: Variation of tangential velocity along y coordinate at z=0 at 200m downstream of turbine for TSR = 8

velocities from this model, like other parameters, coincide with the tangential velocities from CFD-BEMT model.

At TSR = 8, similar behavior is observed for tangential velocities of CFD models except for a few differences. Generally, the tangential velocities are higher at TSR = 8 as compared to those obtained at TSR = 4. CFD-BEMT+LLT M3 shows significantly reduced tangential velocities as compared to those obtained from CFD-BEMT+LLT M1, CFD-BEMT and CFD-BEMT TL in the wake region outwards beyond y = 50 m. This is again due to turbulence mixing. Generally, the wakes for different models at TSR = 8 have expanded more as compared to those at TSR = 4.

7.2.4 Turbulence Kinetic Energy

Figure 28 shows turbulence kinetic energy plotted on *xy*-plane. Plots on left show different CFD models at TSR = 8. Plots on right show CFD-BEMT+LLT M3 method at different TSRs. For CFD-BEMT, CFD-BEMT TL, CFD-BEMT+LLT M1 and CFD-BEMT+LLT M2 models, there is no observable turbulence kinetic energy present at TSR = 8. However, for CFD-BEMT+LLT M3 model, turbulence kinetic energy is seen clearly at TSR = 8

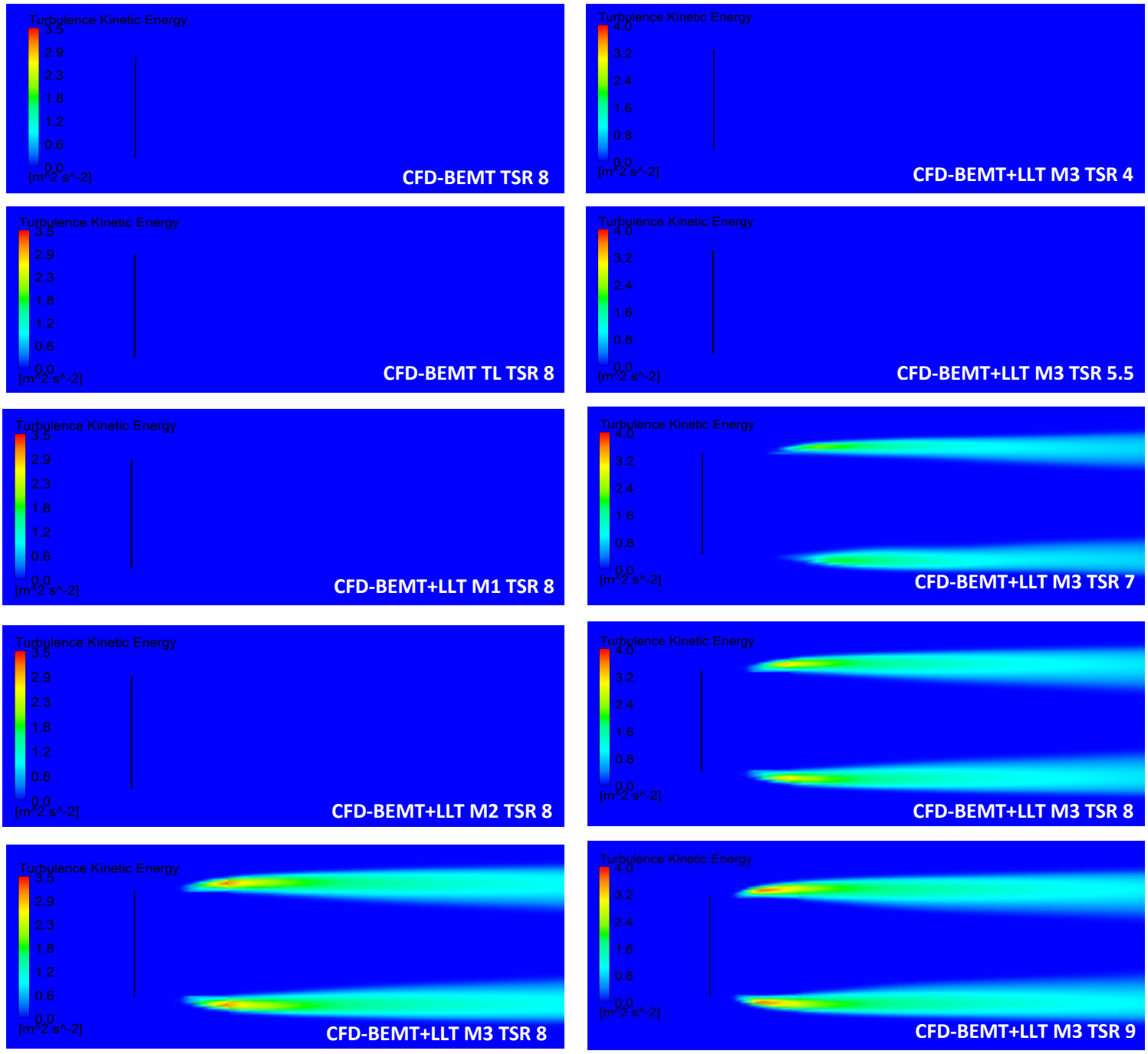

Figure 28: Turbulence kinetic energy plotted on xy-plane . Plots on right show different CFD models at TSR = 8. Plots on left show CFD-BEMT+LLT M3 method at different TSRs

For CFD-BEMT+LLT M3 model at TSR = 8, turbulence kinetic energy is maximum at downstream side near the turbine. As the distance downstream of the turbine increase, turbulence kinetic energy decreases and penetrates towards the center. The plot of axial velocity field at *xy*-plane for CFD-BEMT+LLT M3 model at TSR = 8 shown in Figure 23 also supports this turbulence graph of CFD-BEMT+LLT M3 model at TSR = 8.

The high turbulence is originated in the region where the axial velocity is negative. Negative velocity is caused by high source terms.

From the plots on right side of Figure 28. It is clearly seen that the turbulence level increases with increase in TSR. This is because higher TSRs generate higher magnitudes of additional source terms leading to greater reduction in axial velocity. For TSR = 4 and 5.5, no observable turbulence kinetic energy is achieved for the selected scale. For TSRs = 7, 8 and 9, we can see observable levels in turbulence which increases with TSR.

7.3 Results and discussion for two turbines in a row case

For two turbines in a row case, it is interesting to see how the power and thrust of the downstream wind turbine is effected by the presence of an upstream wind turbine. For this purpose, the second turbine is always set to same TSR of 8 while the TSR of first turbine is changed. The simulations are performed for all five CFD models and the results are compared with each other.

7.3.1 Power and thrust of second turbine

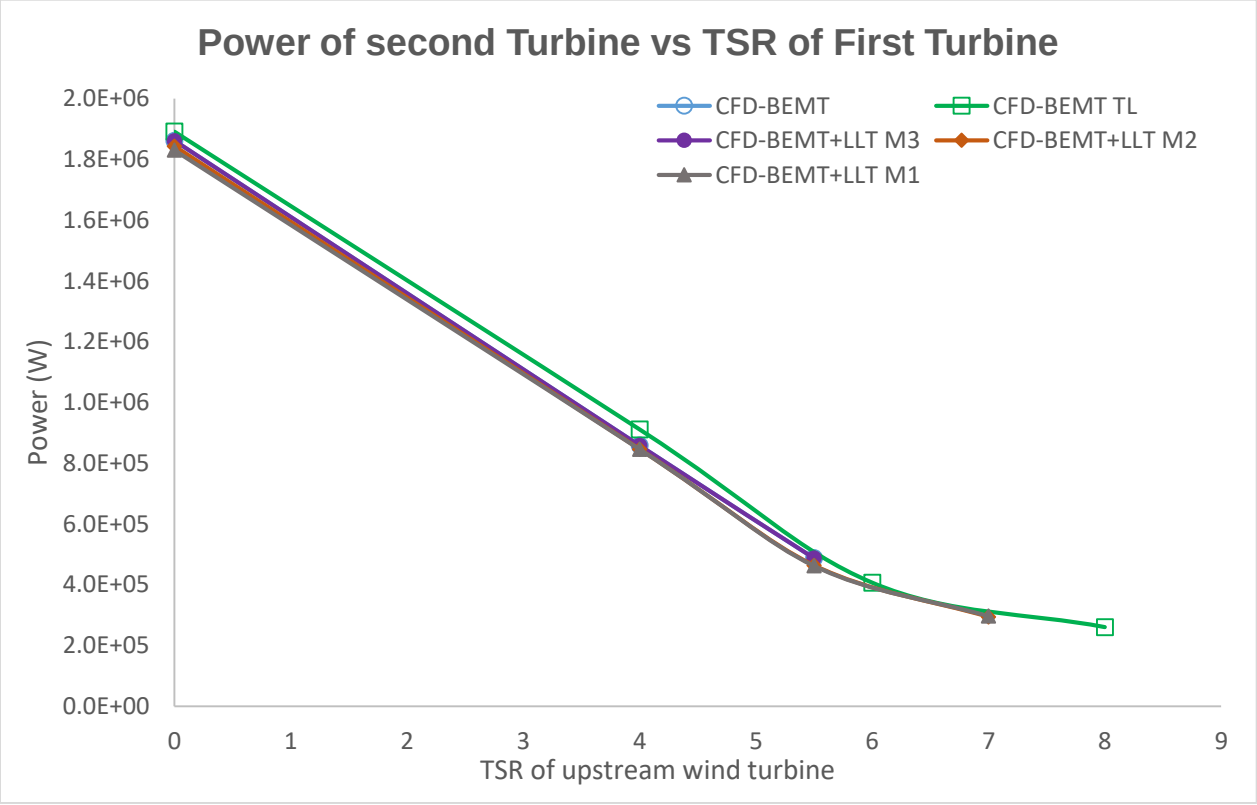

Figure 29: Variation of power of downstream wind turbine with TSR of upstream wind turbine

Figure 29 represents the variation of power of the downstream wind turbine with the TSR of the upstream wind turbine. It is important to notify here that for comparison purpose, results for TSR = 0 corresponds to the cases with single wind turbine (i.e. no upstream wind turbine is present). For all CFD models, the power

of the downstream turbine follows the same general trend with the change in TSR of upstream wind turbine. The power of the downstream wind turbine decrease with the increase in TSR of the upstream wind turbine. For different CFD models, there is not much noticeable difference in the decreasing trend of power with increase in TSR of the upstream wind turbine except that the difference in power predicted from different CFD models diminishes with increase in TSR of first turbine.

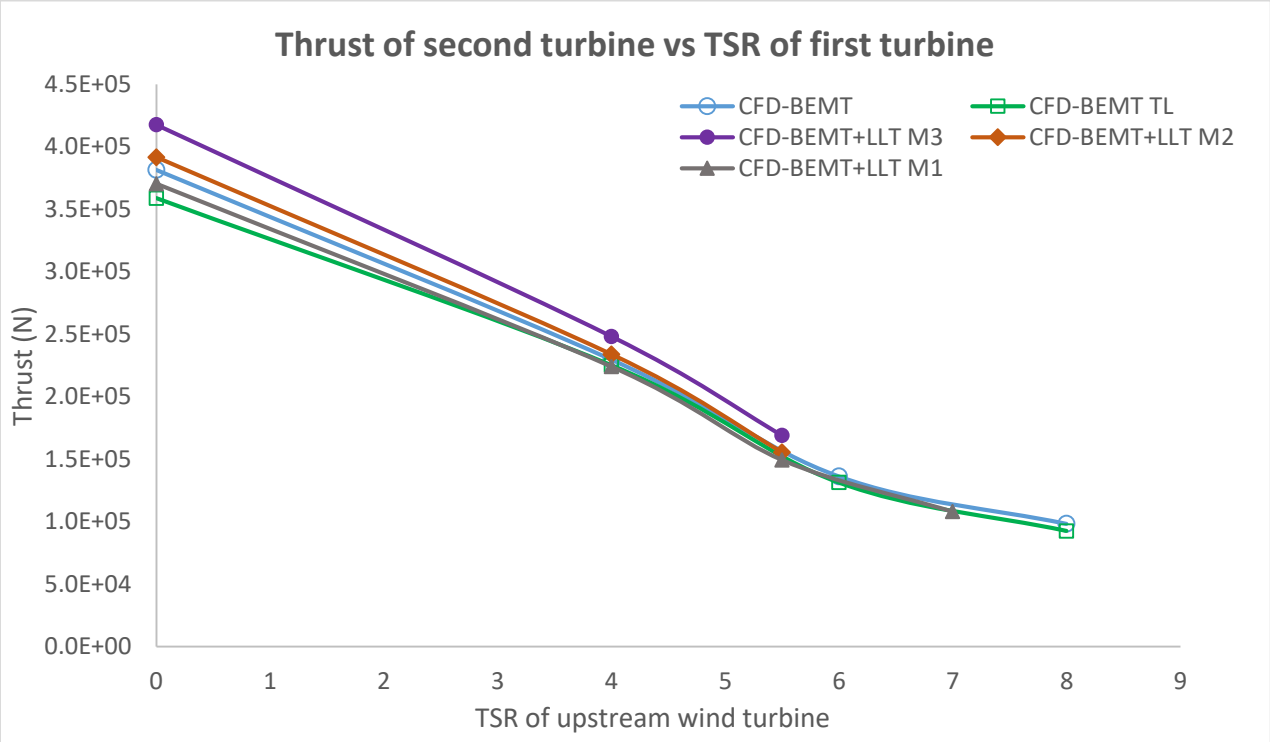

Figure 30: Variation of thrust of downstream wind turbine with TSR of upstream wind turbine

Figure 30 represents the variation of the thrust of the downstream wind turbine with the TSR of the upstream wind turbine. Here again, results for TSR = 0 corresponds to the cases with single wind turbine. For all CFD methods, like power, the thrust of downstream wind turbine shows the same general decreasing trend with increase in TSR of upstream wind turbine. Similarly to the power, for different CFD models, there is not much noticeable difference in the decreasing trend in thrust with increase in TSR of upstream wind turbine except that the difference in thrust predicted from different CFD models diminishes with the increase in TSR of first turbine.

CHAPTER 8: SUMMARY AND CONCLUSION

Three enhanced actuator disc models for CFD analysis of HAWT, CFD-BEMT+LLT M1, CFD-BEMT+LLT M2 and CFD-BEMT+LLT M3, are developed with the intention of simultaneously improving performance and flow field (at tip region) as compared to already existing CFD-BEMT models, with and without tip loss effect. The models are developed by combining the BEMT with the LLT and coupling them to a CFD-RANS model via actuator disc concept. Simulations for a single turbine and two turbines in a row are performed for all five models with the commercial CFD code ANSYS-CFX, which is based on control volume fixed in space approach. Simulation results include performance of wind turbine, local flow field parameters around wind turbine and flow field parameters upstream and downstream of the wind turbine. For comparison of performance results obtained from simulations of single turbine, results from FAST V8 code are used. For comparison of local flow field parameters from the simulations of single turbine, results from LLT IST code are used. Performance results of downstream wind turbine from simulations of two turbines in row are not compared to reference results. In this case, the performance results of the downstream wind turbine with different CFD models are only compared with each other.

None of the enhanced actuator disc model is capable of achieving both the tasks (improving performance and flow field predictions) simultaneously. The three enhanced actuator disc models show very different prediction of flow field at the tip region. Among the three enhanced actuator disc models, for flow field prediction, CFD-BEMT+LLT M1 model shows the worst correlation while CFD-BEMT+LLT M1 model shows the best correlation with the reference results.

CFD-BEMT+LLT M2 and CFD-BEMT+LLT M3 models show too much over prediction in C_T as compared to results obtained from FAST BEMT and FAST BEMT with tip loss throughout the range of TSR presented. There is very narrow range of TSR, TSR = 5.5 to TSR = 7, where the C_P predicted by all the enhanced actuator disc models strongly correlate with the C_P predicted from FAST V8 with tip loss. Outside that range, the enhanced actuator disc models either under predict or over predict $C_{P.}$ Among the three enhanced actuator disc models, for performance prediction, CFD-BEMT+LLT M1 model shows the best correlation while CFD-BEMT+LLT M3 model shows worst correlation with the results obtained from FAST BEMT with tip loss.

Performance predictions from CFD-BEMT TL model show significant difference from the reference performance predictions from FAST BEMT with tip loss. Furthermore, prediction of flow field by CFD-BEMT TL model at the tip region is the worst among all five CFD models used. Clearly, tip loss correction is not a good approach to be incorporated with CFD-BEMT models.

Hence, it can be said that with enhanced actuator disc models, simultaneous improvement in predictions of performance and flow field is not possible. Improvement in performance prediction occurs at the expense of unrealistic predictions of flow field and vice versa.

Only CFD-BEMT+LLT M3 model is capable of producing noticeable turbulence level. Turbulence helps to recover the velocity deficit in the wake. However, the CFD-BEMT+LLT M3 model is not realistic and is only used in this thesis to observe the effect of high momentum source terms in the tip region. But clearly it can be seen that high source terms cause high reductions in axial velocities which lead to turbulence. The enhanced diffusion caused by turbulence is likely to be responsible for the early recover of the wake velocity observed with this model at TSR = 8.

REFERENCES

1. Anderon, J. (2010). *Fundamentals of Aerodynamics* (5 ed.). McGraw-Hill Education.
2. ANSYS, Inc. (2013). *ANSYS CFX Introduction.* Canonsburg, USA.
3. Bai, C. -J., & Wang, W. -C. (2016). Review of computational and experimental approaches to analysis of aerodynamic performance in horizontal-axis wind turbines (HAWTs). *Renewable and Sustainable Energy Reviews, Volume 63*, 506-519.
4. Baltazar, J., Machado, J., & Falcão de Campos, J. (2011). HYDRODYNAMIC DESIGN AND ANALYSIS OF HORIZONTAL AXIS MARINE. *Proceedings of the ASME 2011 30th International Conference on Ocean, Offshore and Arctic Engineering.* Rotterdam, France.
5. Barahona, B., Jonkman, J., Damiani, R., Robertson, A., & Hayman, G. (2014). *Verification of the New FAST v8 Capabilities for the Modeling of Fixed-Bottom Offshore Wind Turbines.* United States: National Renewable Energy Laboratory.
6. Burton , T., Sharpe, D., Jenkins, N., & Bossanyi, E. (2001). *Wind Energy Handbook.* Wiley.
7. Edmunds, M., Williams, A. J., Masters, I., & Croft, T. N. (2015). BEM-CFD: A Revised Model for Accurate Prediction. *Proceedings of the 11th European Wave and Tidal Energy Conference.* Nantes.
8. Esfahanian, V., Salavati Pour, A., Harsini, I., Haghani, A., Pasandeh, R., Shahbazi, A., & Ahmadi, G. (2013). Numerical analysis of flow field around NREL Phase II wind turbine by a hybrid CFD/BEM method. *Wind Engineering and Industrial Aerodynamics, 120*, 29-36.
9. Hansen, M. O. (2008). *Aerodynamics of Wind Turbines (Second Edition).* London: Earthscan.
10. Iowa Energy Center. (2016). *History of Wind Energy*. Retrieved from Iowa Energy Center: http://www.iowaenergycenter.org/wind-energy-manual/history-of-wind-energy
11. Jonkman, J., Butterfield, S., Musial, W., & Scott, G. (2009). *Definition of a 5-MW Reference Wind Turbine for Offshore System Development.* National Renewable Energy Laboratory.
12. Manwell, J. F., Mcgowan, J. G., & Rogers, A. L. (2009). *Wind Energy Explained: Theory, Design and Application, 2nd Edition.* London: Wiley.
13. Mehta, D., van Zuijlen, A. H., Koren, B., Holierhoek, J. G., & Bijl, H. (2014). Large Eddy Simulation of wind farm aerodynamics: A review. *Wind Engineering and Industrial Aerodynamics*, 1-17.
14. Moriarty, P. J., & Hansen, A. C. (2005). *AeroDyn Theory Manual.* National Renewable Energy Laboratory.
15. Von Mises, R. (1959). *Theory of Flight.* Dover Publications.
16. Wind Energy Foundation. (2016). *History of Wind Energy*. Retrieved from Wind Energy Foundation.
17. Wu, Y. -T., & Porté-Agel, F. (2015). Modeling turbine wakes and power losses within a wind farm using LES: An application to the Horns Rev offshore wind farm. *Renewable Energy*, 945-955.